Hydrodynamic performance of a self-protected hybrid offshore wind-wave energy system

Cong, Peiwen
State Key Laboratory of Coastal and Offshore Engineering, Dalian University of Technology

Liu, Yingyi
Research Institute for Applied Mechanics, Kyushu University

Wei, Xuanqi
State Key Laboratory of Coastal and Offshore Engineering, Dalian University of Technology

Ning, Dezhi
State Key Laboratory of Coastal and Offshore Engineering, Dalian University of Technology

他

https://hdl.handle.net/2324/6796348

出版情報：Physics of Fluids. 35 (9), pp.097107-, 2023-09-06. American Institute of Physics : AIP
バージョン：
権利関係：

Hydrodynamic performance of a self-protected hybrid offshore wind-wave energy system

Peiwen Cong(丛培文) [a], *Yingyi Liu*(刘盈溢) [b,*], *Xuanqi Wei*(卫轩旗)[a], *Dezhi Ning*(宁德志) [a] and *Bin Teng*(滕斌) [a]

[a] State Key Laboratory of Coastal and Offshore Engineering, Dalian University of Technology, Dalian 116024, China

[b] Research Institute for Applied Mechanics, Kyushu University, Fukuoka 8168580, Japan

Abstract

The load-bearing capacity is a pivotal consideration in the design of offshore renewable energy structures. This paper aims to address the technical challenges associated with the additional wave loads caused by the integrated devices in a hybrid system for the multi-purpose utilization of coastal renewable energy. A self-protected hybrid wind-wave energy system is proposed, in which an oscillating water column (OWC) device is attached at a monopile foundation of an offshore wind turbine. In the meantime, the OWC is connected by a submerged horizontal perforated plate at its exterior shell, which is expected to minimize the wave loads on the system. The hydrodynamic performance of the system is investigated. A novel approach is developed to model the wave interaction with the hybrid system. This efficient approach removes the necessity of decomposing the wave-scattering field into diffraction and pressure-dependent radiation components. Detailed numerical computation is then conducted for both regular and irregular sea states. Various hydrodynamic properties related to the system, such as wave energy harvesting, wave force/moment and free-surface elevation, have been evaluated. Numerical results manifest the feasibility of imposing a negligible effect on the high wave energy harvesting while reducing the high wave loads by manipulating the submerged horizontal perforated plate. The impact of the perforated plate on the

---

[*] Corresponding author.

E-mail addresses: pwcong@dlut.edu.cn (P. Cong), liuyingyi@riam.kyushu-u.ac.jp (Y. Liu), xqwei@mail.dlut.edu.cn (X. Wei), dzning@dlut.edu.cn (D. Ning), bteng@dlut.edu.cn (B. Teng).

dominant wave energy harvesting in the long-period region is found to be trivial. In contrast, it can affect the high bending moment in the short-period region, which causes a reduction of greater than 15%.

Keywords: hybrid system; monopile foundation; horizontal perforated plate; oscillating water column (OWC)

1. Introduction

The high installation and transmission cost has been the primary challenge in reaching a viable commercial stage in offshore energy (wind or wave) farms (Jiang et al., 2018). Efficient solutions are required to increase the expected revenue and offer more cost-share opportunities. Due to the concomitant relationship between offshore winds and ocean waves, wave energy may also be of considerable amount where the offshore wind energy resource is rich. Therefore, it is appealing to integrate different technologies into one single platform. Such a combination may have several noticeable advantages, including better utilization of ocean space, decreasing the cost relevant to the operation, maintenance, foundation substructure and the required electric grid infrastructure (Karimirad, 2014), and enhancing ocean energy dispatchability (Gao et al., 2023). Meanwhile, the power can be generated from a mixture of offshore-wind turbines and wave generators. Then, when a wind turbine operating at low wind speeds outputs a power level lower than the rated, the power shortage can be compensated by utilizing wave energy converters (Zhang et al., 2022).

Due to the significant opportunities and benefits, the integration of different technologies of offshore energy has attracted much attention from researchers. Those combined systems can generally be realized in two different forms according to the connectivity. When the system is designed to integrate wind turbine units and wave energy converters into a shared platform, it is typically classified as a hybrid system (Pérez-Collazo et al., 2018). A hybrid system is part of the broader family of multi-purpose platforms. Currently, many inventive concepts of hybrid systems have been proposed. Typical examples include the integration of an oscillating buoy or buoy array with a semisubmersible-type or a spar-type wind turbine (Muliawan et al., 2013; Cheng et al., 2019; Ren et al., 2020; Hu et al., 2020; Li et al., 2022a; Meng et al., 2023), integration of an oscillating water column (OWC) device or OWC array into a floating or bottom-mounted offshore wind turbine (Perez-Collazo et al., 2018; Michele et al., 2019; Sarmiento et al., 2019; Zhou et al., 2020; Cong et al., 2021; Dimitrios et al., 2021; Li et al., 2022b; Zhang et al., 2022) and a semisubmersible type wind turbine combined with flap-type wave energy converters (Luan et al., 2014; Michailides et al., 2016a, 2016b). The concept feasibility of different hybrid systems has been assessed.

Existing offshore wind turbines mainly comprise wind turbines with fixed foundations installed (Wang et al., 2019). Due to its ease of manufacture, installation and economy, the monopile foundation has been one of the most popular support structures for fixed offshore wind turbines. In the meantime, among different classes of designs of wave energy converters, the OWC device has been considered one of the most promising options, with the largest number of prototypes so far deployed into the sea. It suggests that integrating an OWC with a monopile foundation of a wind turbine can be a promising way for the multi-purpose utilization of offshore renewable energy and hence attract the interest of many researchers. The hybrid concepts, where the OWC is mounted on a monopile foundation or a jacket frame, were proposed by Perez-Collazo et al. (2018). A comprehensive set of experimental campaigns have been conducted to analyze the reflected waves, capture width ratio, free surface elevation and wave runup. The hydrodynamic behaviour of the system in regular and irregular waves has been investigated. Michele et al. (2019) developed an analytical solution for a hybrid wind-wave energy system in which the OWC is coaxial with the monopile foundation, and its exterior shell has a skirt structure. The wave interaction with a monopile-mounted wind turbine surrounded by an external OWC is experimentally studied by Zhou et al. (2020). Independent foundations were used for the wind turbine and wave energy converter. Experimental results showed that the external OWC could impose a shielding effect on the internal monopile foundation and, in turn, reduce the wave loads on the foundation. The wave power absorption by a multi-chamber OWC integrated into a monopile foundation was numerically investigated by Cong et al. (2021). A self-adaptive Gauss integration method was developed for OWCs (Cong et al., 2022), providing an efficient solution to the nearly singular integration caused by the existence of thin elements, such as the external shell of the OWC and internal stiffening plates. Numerical results illustrated that a significant energy extraction efficiency is attained when remarkable piston-like wave motion is induced within each sub-chamber, and the air compressibility negatively affects the wave power absorption. For the system proposed by Li et al. (2022b), two openings were made on the side wall of the monopile foundation. The submerged opening allows ambient waves to propagate inside, while an air duct housing an air turbine is installed on the higher opening above the free surface. Experimental results revealed that a shallower submergence depth of the opening beneath the free surface leads to a broader efficiency band.

Apart from the self-weight and operation of the installed machinery, offshore foundations are subjected to the cyclic loads generated by environmental conditions. In the ocean environment, one of the primary sources of the variable loads is the hydrodynamic. For monopile foundations, the monopile's lateral deflection (rotation) controls the structure's serviceability limit state (Arshad and O'Kelly, 2016). A reduction of the wave loads on structures is beneficial to the improvement of structure survivability. Perforated structures have been widely used in coastal and offshore engineering to mitigate wave impact (Huang et al., 2011). The horizontal perforated plate is a typical type of perforated structure, and it has been used as the critical element of breakwaters since the 1990s (Yu and Chwang, 1994). The perforated horizontal plate is economically friendly and can meet different practical requirements. It can be designed as either a floating or pile-supported type (Li et al., 2022c), less dependent on seabed conditions and water depths. In addition, a perforated horizontal plate, which is submerged at a certain distance below the free surface, can maintain the wave reflection and transmission at a low level (Li et al., 2006). Meanwhile, it can avoid the heavy horizontal wave load acting on the structure (Zhao et al., 2017). Furthermore, a perforated flat plate enables the exchange of water below and above it, thus preventing seawater pollution and protecting water quality (Cho and Kim, 2013). Various research has been conducted on wave interaction with horizontal perforated plates. Its hydrodynamic characteristics (i.e., coefficients of wave reflection, transmission, energy dissipation and wave force) related to variations in plate size, spacing, submerged depth, inclination angle, and incident wavelength have been widely discussed. Examples include Cho and Kim (2008), Evans and Peter (2011), Liu et al. (2008, 2012), Vijay et al. (2020), Liang et al. (2021), Poguluri et al. (2022) and Zheng et al. (2023). The above studies focus on rigid perorated plates. The wave scattering and energy dissipation by perforated elastic plates has been investigated by researchers using the eigenfunction-matching method (Meylan et al., 2017; Zheng et al., 2020a, 2020b) or deriving an extension formulae with the aid of Green's function technique (Mohapatra et al., 2018). Recently, the application of a perforated elastic plate or plate array as a power take-off (PTO) device to harvest wave energy has been discussed by Liang et al. (2022).

The combined wind-wave energy system presents a cost-competitive advantage but also has the technical challenge that the addition of the wave energy system tends to cause additional wave loads on the wind turbine foundation. Encouraged by the favourable performance of the submerged horizontal perforated plate as a breakwater, it is believed that integrating the perforated plate into the hybrid system can be a promising way to address this challenge. In view of this, a self-protected hybrid offshore wind-wave energy system is proposed in this research. 'self-protected' refers to the ability of the device to protect itself from excessive wave loads. Detailed numerical studies are then conducted for the hydrodynamic performance of the system by drawing on a newly developed numerical model. The effect of the perforated plate on the wave energy harvesting and the wave loads on the system has been discussed in detail.

The remaining part of the paper is organized as follows. First, a description of the hybrid system is given in Section 2. Then, the hydrodynamic problem and power take-off model are presented in Section 3. In Section 4, the solution to the defined boundary-value problem is introduced in detail. Then, a numerical investigation is carried out in Section 5. Finally, conclusions are drawn in Section 6 based on the previous analysis.

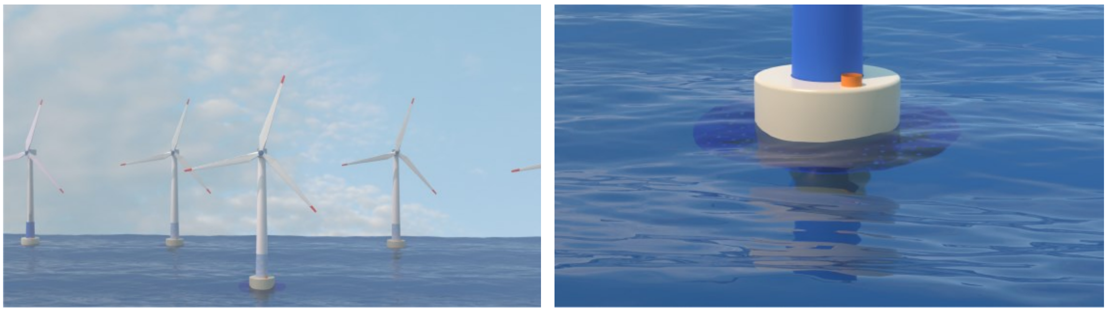

Fig. 1 Computer graph of the hybrid wind-wave system: (left) bird's-eye view of the floating wind farm, and (right) local magnification of the OWC-type device.

2. Description of the hybrid system

An overview of the hybrid system is given in Fig. 1, where an OWC-type wave energy converter is mounted on a monopile-type offshore wind turbine substructure. The monopile is the most common offshore wind substructure system. Offshore wind turbines with monopiles have a broad range in terms of power ratings. As shown in Fig. 1, the OWC is coaxial with the monopile foundation that penetrates the seabed and shares the foundation with an offshore wind turbine. The OWC consists of a partly submerged air chamber with the bottom open to the sea. The air chamber is of an annular cross-section. Consequently, the OWC, which forms the wave energy converter sub-system, can self-adapt to an arbitrary wave direction due to the symmetry of the device.

The monopile foundation and the air chamber shell enclose an interior-free surface subject to reciprocating air pressure. A submerged ring-shaped horizontal perforated plate is attached to the chamber's shell. Such a shape of the perforated plate manages to mitigate the wave impact from all wave directions. The chamber is connected with the outer atmosphere through the air duct installed on the roof of the chamber. The air duct houses an air turbine (e.g., a Wells turbine). In a typical OWC, the moving mechanical part is the air turbine above the water surface. It acts as the OWC power take-off device, driving the electric generator to produce electricity. The exterior and interior free surfaces are at the same level initially, and an amount of air is entrapped above the interior free surface.

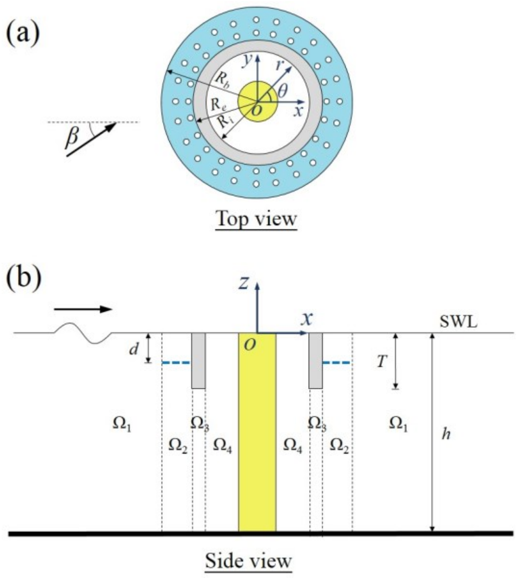

Fig. 2 Definition of the coordinate systems and subdomains: (a) top view and (b) side view.

3. Hydrodynamic problem and power take-off model

Fig. 2 shows the idealized sketch of the submerged part of the system. The radius of the monopile is a, and the draft of the OWC is T. For the exterior shell of the OWC, its inner and outer radii are R_i and R_e, respectively. The perforated plate is attached at a submergence depth of d, and its width equals $b = R_b - R_e$, where R_b is its exterior radius. The system is subjected to incident waves propagating along the positive x-direction. The water depth is assumed to be constant and denoted by h. The present physical problem is formulated by defining the Cartesian and cylindrical coordinate systems, with the oxy and $or\theta$ planes at the still free surface and the z-axis vertical upward.

The present problem is solved in the context of potential flow theory, where the fluid is assumed to be incompressible, and its motion is irrotational. Then, there exists a velocity potential $\Phi(\mathbf{x};\, t)$ satisfying Laplace's equation that can describe the fluid motion. Here, $\mathbf{x} = (x, y, z)^T$ is the position vector. For linear small-amplitude harmonic incident waves with the angular frequency ω, the velocity potential will have the following form

$$\Phi(\mathbf{x};\, t) = \mathrm{Re}\left[\phi(\mathbf{x}) e^{-\mathrm{i}\omega t}\right], \tag{1}$$

where 'Re' denotes the real part of a complex function.

Besides the governing equation, the velocity potential should satisfy appropriate boundary conditions. The exterior free surface S_e ($r \geq R_e$) is subjected to the constant atmospheric pressure P_0, which is assumed to be zero. While there is a distribution of air pressure $P_0 + P_c(t)$ above the interior free surface. $P_c(t)$ is the air pressure oscillating at the same frequency as the incident waves. Then, it has the following form

$$P_c(t) = \mathrm{Re}\left[p_c e^{-\mathrm{i}\omega t}\right], \tag{2}$$

where p_c is the complex amplitude of the oscillating air pressure. Then, on $z = 0$, the combined kinematic and dynamic boundary condition is given by

$$\frac{\partial \phi}{\partial z} - \frac{\omega^2}{g}\phi = \frac{\mathrm{i}\omega}{\rho g} p_c, \quad \text{on } S_i; \tag{3a}$$

$$\frac{\partial \phi}{\partial z} - \frac{\omega^2}{g}\phi = 0, \quad \text{on } S_e. \tag{3b}$$

On the impermeable body surface and seabed, the boundary conditions are given by

$$\frac{\partial \phi}{\partial n} = 0, \quad \text{on } S_b, \tag{4}$$

and

$$\frac{\partial \phi}{\partial z} = 0, \quad \text{on } z = -h, \tag{5}$$

where S_b represents the mean wetted surface of the air chamber and the monopile foundation; **n** is the normal unit vector pointing outward from the fluid domain.

In addition, it is assumed that the perforated plate is made of material with fine pores, and the normal velocity of the fluid passing through the plate is linearly proportional to the pressure difference between the two sides of the plate (Chwang, 1983). Then, the following boundary conditions can be derived

$$\frac{\partial \phi}{\partial z} = \mathrm{i}\sigma\left(\phi^- - \phi^+\right), \quad \left(z = -d;\ R_e \leq r \leq R_e + b\right) \tag{6}$$

where σ is the porous-effect parameter; the subscripts '+' and '–' are used to denote the potentials on the upper and lower surfaces of the plate.

The porous-effect parameter σ varies from 0 to infinity with a dimension of reciprocal metre. When it is equal to 0, it is impermeable. Contrarily, as it goes to infinity, the surface becomes completely permeable. The real and imaginary parts of σ represent the resistance and inertial effects of the perforated plate, respectively. Previous experimental studies of Li et al. (2006) suggested that the real part of σ dominates over the imaginary part.

By a set of experiments, Zhao et al. (2011) defined a parameter B_0, and connected it to the porous-effect parameter σ and the opening rate τ of the material, obtaining

$$B_0 = \sigma \cdot \frac{2\pi}{\kappa_0} = \frac{\left(\frac{17.8}{\kappa_0 A} + 143.2\right)\tau^2}{1 + 1.06\tau}, \tag{7}$$

in which A is the incident wave amplitude; κ_0 is the real wave number. The wave number κ_0 and the wave frequency ω satisfy a dispersion relation $\omega^2 = g\kappa_0 \tanh(\kappa_0 h)$ in which g is the gravitational acceleration.

The wave scattering by the horizontal perforated plates has been experimentally investigated in previous studies, such as Cho and Kim (2008, 2013). In the former, the plate porosity rate τ varies from 5.67% to 40.31%, while in the latter form 8.0% to 33.0%. A perforated plate with a high porosity may experience an elastic response under wave action. However, in the experiments of Cho and Kim (2008, 2013), elastic response of the plate has not been observed. In view of this, $\tau = 40.0\%$ is used as a threshold for a perforated rigid plate in this study. We then concern the scenario in a water depth of $h = 20$ m, and the incident waves have unit wave height. Meanwhile, the perforated plate adopted by the system has a porosity rate of $\tau = 40.0\%$. Then, when the wave period varies from 2.0 s to 20.0 s, the porous-effect parameter σ (determined based on Eq. (7)) changes from 0.70 m^{-1} to 3.19 m^{-1}. It suggests that a porous-effect parameter of $\sigma = 0.50$ m^{-1} is sufficient to ensure the present results free from the influence of elastic response. Therefore, $\sigma = 0.50$ m^{-1} has been used in the subsequent study unless otherwise stated.

At a large distance from the structure, the following Sommerfeld radiation condition should be satisfied:

$$\lim_{r \to +\infty} \left\{ \sqrt{r} \left[\frac{\partial}{\partial r}(\phi - \phi_I) - \mathrm{i}\kappa_0 (\phi - \phi_I) \right] \right\} = 0, \tag{8}$$

in which $\phi_I(\mathbf{x})$ is the incident potential and given by

$$\phi_I(\mathbf{x}) = -\frac{\mathrm{i}Ag}{\omega}\frac{\cosh\left[\kappa_0(z+h)\right]}{\cosh(\kappa_0 h)}\mathrm{e}^{\mathrm{i}\kappa_0 x}. \tag{9}$$

In this study, a Wells-type turbine is employed for the power take-off. Referring to Martins-Rivas and Mei (2009), the relationship between the air volume flux inside the chamber and the oscillating air pressure can be expressed as:

$$p_c = \Lambda q_c, \tag{10}$$

where q_c is the complex amplitude of the air volume flux; the pneumatic damping coefficient Λ is defined by:

$$\Lambda = \frac{1}{\chi - \mathrm{i}\omega\mu}. \tag{11}$$

In Eq. (11), χ and μ are normally defined as the turbine and chamber parameters, respectively. χ can be adjusted in some ways, such as varying the rotational speed N of the air turbine. μ represents the effect of the air compressibility in the chamber. χ and μ are defined by:

$$\chi = \frac{KD}{N\rho_a}; \tag{12a}$$

$$\mu = \frac{V_0}{c^2\rho_a}. \tag{12b}$$

where K is an empirical coefficient depending on the design of the air turbine; D is the diameter of the turbine rotor; c is the sound speed in the air; ρ_a is the air density; V_0 is the volume of the entrapped air in the chamber in still water. Then, Eq. (3a) can be written as

$$\frac{\partial\phi}{\partial z} - \frac{\omega^2}{g}\phi = \frac{\mathrm{i}\omega\Lambda}{\rho g}\iint_{S_i}\frac{\partial\phi}{\partial z}\mathrm{d}s, \quad \text{on } S_i. \tag{13}$$

The captured power W_c is the time-averaged rate of work done by the oscillating air pressure pushing the air through the air turbine (Evans and Porter, 1997). That is

$$W_c = \frac{1}{2}\mathrm{Re}\left[p_c q_c\right] = \frac{1}{2}\chi\left|p_c\right|^2. \tag{14}$$

4. Solution method to the boundary value problem

The solution to the established boundary value problem is derived in this section. The whole fluid domain is divided into four subdomains: Ω_1, Ω_2, Ω_3 and Ω_4, as shown in Fig. 2. Ω_1 is the exterior subdomain ($r \geq R_b$, $-h \leq z \leq 0$); Ω_2 is the subdomain containing the perforated plate ($R_e \leq r \leq R_b$, $-h \leq z \leq 0$); Ω_3 is the subdomain underneath the chamber shell ($R_i \leq r \leq R_e$, $-h \leq z \leq -T$); Ω_4 is the interior subdomain ($a \leq r \leq R_i$, $-h \leq z \leq 0$). Hereinafter, ϕ_n ($n = 1, 2, 3, 4$) is used to denote the spatial velocity potential in the nth subdomain.

The solution procedure starts by deriving the expressions for the velocity potential in each subdomain. The boundary condition on the free surface in Ω_4 is inhomogeneous. A particular solution satisfying the inhomogeneous boundary condition is to be determined in Ω_4. An eigenfunction expansion of the spatial potential can be obtained using the method of separation of variables. After expanding it into the Fourier-cosine series in the angular direction, the velocity potential can be expressed in the form of orthogonal series in each subdomain (Michele et al., 2019):

$$\phi_1(r,\ z,\ \theta) = -\frac{\mathrm{i}Ag}{\omega}\sum_{m=0}^{+\infty}\left\{\varepsilon_m \mathrm{i}^m\left[J_m(\kappa_0 r)Z_0(\kappa_0 z)\sqrt{N_0} + \sum_{j=0}^{+\infty}A_{m,j}R_{m,j}(\kappa_j r)Z_j(\kappa_j z)\right]\cos m\theta\right\};$$

$$(15a)$$

$$\phi_2(r,\ z,\ \theta) = -\frac{\mathrm{i}Ag}{\omega}\sum_{m=0}^{+\infty}\left\{\varepsilon_m \mathrm{i}^m\sum_{l=0}^{+\infty}\left[B_{m,\,l}P_{m,\,l}(\mu_l r) + C_{m,\,l}Q_{m,\,l}(\mu_l r)\right]U_l(\mu_l z)\cos m\theta\right\}; \quad (15b)$$

$$\phi_3(r,\ z,\ \theta) = -\frac{\mathrm{i}Ag}{\omega}\sum_{m=0}^{+\infty}\left\{\varepsilon_m \mathrm{i}^m\sum_{k=0}^{+\infty}\left[D_{m,\,k}S_{m,\,k}(\lambda_k r) + E_{m,\,k}T_{m,\,k}(\lambda_k r)\right]Y_k(\lambda_k z)\cos m\theta\right\}; \quad (15c)$$

$$\phi_4(r,\ z,\ \theta) = -\frac{\mathrm{i}Ag}{\omega}\sum_{m=0}^{+\infty}\left\{\varepsilon_m \mathrm{i}^m\sum_{j=0}^{+\infty}F_{m,j}W_{m,j}(\kappa_j r)Z_j(\kappa_j z)\cos m\theta\right\} + \phi_p. \quad (15d)$$

where $A_{m,j}$, $B_{m,\,l}$, $C_{m,\,l}$, $D_{m,\,k}$, $E_{m,\,k}$ and $F_{m,j}$ are the Fourier expansion coefficients, and to be determined.

In the expression of the velocity potential in Ω_1 and Ω_4 (see Eqs. (15a) and (15d)), the radial and vertical eigenfunctions $R_{m,j}(\kappa_j r)$, $W_{m,j}(\kappa_j r)$ and $Z_j(\kappa_j z)$ are given by the following forms:

$$R_{m,j}\left(\kappa_j r\right)=\begin{cases}\dfrac{H_m\left(\kappa_0 r\right)}{H_m\left(\kappa_0 R_b\right)}, & j=0,\\[2ex] \dfrac{K_m\left(\kappa_j r\right)}{K_m\left(\kappa_j R_b\right)}, & j\geq 1;\end{cases}\tag{16a}$$

$$W_{m,j}\left(\kappa_j r\right)=\begin{cases}\dfrac{J_m\left(\kappa_0 r\right)H'_m\left(\kappa_0 a\right)-J'_m\left(\kappa_0 a\right)H_m\left(\kappa_0 r\right)}{J_m\left(\kappa_0 R_i\right)H'_m\left(\kappa_0 a\right)-J'_m\left(\kappa_0 a\right)H_m\left(\kappa_0 R_i\right)}, & j=0,\\[2ex] \dfrac{I_m\left(\kappa_j r\right)K'_m\left(\kappa_j a\right)-I'_m\left(\kappa_j a\right)K_m\left(\kappa_j r\right)}{I_m\left(\kappa_j R_i\right)K'_m\left(\kappa_j a\right)-I'_m\left(\kappa_j a\right)K_m\left(\kappa_j R_i\right)}, & j\geq 1,\end{cases}\tag{16b}$$

and

$$Z_j\left(\kappa_j z\right)=\begin{cases}\dfrac{\cosh\left[\kappa_0\left(z+h\right)\right]}{\cosh\left(\kappa_0 h\right)}\dfrac{1}{\sqrt{N_0}}, & j=0,\\[2ex] \dfrac{\cos\left[\kappa_j\left(z+h\right)\right]}{\cos\left(\kappa_j h\right)}\dfrac{1}{\sqrt{N_j}}, & j\geq 1.\end{cases}\tag{17}$$

with

$$N_j=\begin{cases}\dfrac{1}{\cosh^2\left(\kappa_0 h\right)}\dfrac{h}{2}\left[1+\dfrac{\sinh\left(2\kappa_0 h\right)}{2\kappa_0 h}\right], & j=0,\\[2ex] \dfrac{1}{\cos^2\left(\kappa_j h\right)}\dfrac{h}{2}\left[1+\dfrac{\sin\left(2\kappa_j h\right)}{2\kappa_j h}\right], & j\geq 1.\end{cases}\tag{18}$$

In Eqs. (16), (17) and (18), κ_j ($j \geq 1$) is the positive real roots of $-\omega^2 = g\kappa_j \tan\left(\kappa_j h\right)$; $H_m(\cdot)$ is the Hankel function; $K_m(\cdot)$ is the modified Bessel function of the second kind. From Eq. (16), the Sommerfeld radiation and the no-flow conditions at $r = a$ have been well respected. Eq. (17) ensures that the boundary conditions on the mean plane of the free surface ($z = 0$) and the seabed ($z = -h$) are well satisfied. In addition, the particular solution ϕ_p in Eq. (15d) is derived as

$$\phi_p=-\frac{2\pi A\Lambda}{\rho}\sum_{j=0}^{+\infty}\left(\frac{F_{0,j}}{\sqrt{N_j}}\Pi_j\right),\tag{19}$$

in which,

$$\Pi_j=\begin{cases}\dfrac{\left[J_1\left(\kappa_0 R_i\right)R_i-J_1\left(\kappa_0 a\right)a\right]H'_0\left(\kappa_0 a\right)-\left[H_1\left(\kappa_0 R_i\right)R_i-H_1\left(\kappa_0 a\right)a\right]J'_0\left(\kappa_0 a\right)}{\kappa_0\left[J_0\left(\kappa_0 R_i\right)H'_0\left(\kappa_0 a\right)-J'_0\left(\kappa_0 a\right)H_0\left(\kappa_0 R_i\right)\right]}, & j=0,\\[2ex] \dfrac{\left[I_1\left(\kappa_j R_i\right)R_i-I_1\left(\kappa_j a\right)a\right]K'_0\left(\kappa_j a\right)+\left[K_1\left(\kappa_j R_i\right)R_i-K_1\left(\kappa_j a\right)a\right]I'_0\left(\kappa_j a\right)}{\kappa_j\left[I_0\left(\kappa_j R_i\right)K'_0\left(\kappa_j a\right)-I'_0\left(\kappa_j a\right)K_0\left(\kappa_j R_i\right)\right]}, & j\geq 1.\end{cases}\tag{20}$$

In the expression of the velocity potential in Ω2 (see Eq. (15b)), the radial function is given by the following form

$$P_{m,l}(\mu_l r)=\begin{cases}\dfrac{J_m(\mu_0 r)H_m(\mu_0 R_e)-J_m(\mu_0 R_e)H_m(\mu_0 r)}{J_m(\mu_0 R_b)H_m(\mu_0 R_e)-J_m(\mu_0 R_e)H_m(\mu_0 R_b)}, & l=0,\\[2ex] \dfrac{I_m(\mu_l r)K_m(\mu_l R_e)-I_m(\mu_l R_e)K_m(\mu_l r)}{I_m(\mu_l R_b)K_m(\mu_l R_e)-I_m(\mu_l R_e)K_m(\mu_l R_b)}, & l\geq 1;\end{cases} \tag{21a}$$

$$Q_{m,l}(\mu_l r)=\begin{cases}\dfrac{J_m(\mu_0 R_b)H_m(\mu_0 r)-J_m(\mu_0 r)H_m(\mu_0 R_b)}{J_m(\mu_0 R_b)H_m(\mu_0 R_e)-J_m(\mu_0 R_e)H_m(\mu_0 R_b)}, & l=0,\\[2ex] \dfrac{I_m(\mu_l R_b)K_m(\mu_l r)-I_m(\mu_l r)K_m(\mu_l R_b)}{I_m(\mu_l R_b)K_m(\mu_l R_e)-I_m(\mu_l R_e)K_m(\mu_l R_b)}, & l\geq 1.\end{cases} \tag{21b}$$

In addition, the depth-dependent function $U_l(\mu_l z)$ is derived based on the method proposed by Yu and Chwang (1994). Then, we can obtain that

$$U_l(\mu_l z)=\begin{cases}\sinh\left[\mu_l(h-d)\right]\cdot\left[\dfrac{\omega^2}{g}\sinh(\mu_l z)+\mu_l\cosh(\mu_l z)\right]\dfrac{1}{\sqrt{M_l}}, & -d\leq z\leq 0,\\[2ex] \cosh\left[\mu_l(z+h)\right]\cdot\left[\dfrac{\omega^2}{g}\cosh(\mu_l d)-\mu_l\sinh(\mu_l d)\right]\dfrac{1}{\sqrt{M_l}}, & -h\leq z\leq -d,\end{cases} \tag{22}$$

with

$$\begin{aligned}M_l=&\frac{1}{2}\sinh^2\left[\mu_l(h-d)\right]\cdot\left\{\left[\left(\frac{\omega^2}{g}\right)^2+(\mu_l)^2\right]\frac{\sinh(2\mu_l d)}{2\mu_l}+\left[\mu_l^2-\left(\frac{\omega^2}{g}\right)^2\right]\cdot d-2\frac{\omega^2}{g}\sinh^2(\mu_l d)\right\}\\&+\frac{1}{2}\left\{\frac{1}{2\mu_l}\sinh\left[2\mu_l(h-d)\right]+(h-d)\right\}\cdot\left[\left(\frac{\omega^2}{g}\right)\cosh(\mu_l d)-\mu_l\sinh(\mu_l d)\right]^2.\end{aligned} \tag{23}$$

In Eqs. (22) and (23), the complex wave number μ_l satisfies the following complex dispersion relation

$$\begin{aligned}&\mu_l\sinh\left[\mu_l(h-d)\right]\cdot\left[\frac{\omega^2}{g}\cosh(\mu_l d)-\mu_l\sinh(\mu_l d)\right]\\&=\mathrm{i}\sigma\left[\frac{\omega^2}{g}\cosh(\mu_l h)-\mu_l\sinh(\mu_l h)\right],\quad l=0,\ 1,\ 2,\ \ldots.\end{aligned} \tag{24}$$

Eq. (24) is derived based on the boundary condition at $z = 0$, $-d$ and $-h$ in Ω2, respectively. The roots of the complex dispersion relations, Eq. (24), are determined using an iterative method in conjunction with the Taylor series expansion.

In the expression of the velocity potential in Ω_3 (see Eq. (15c)), the radial and vertical eigenfunctions $S_{m,k}(\lambda_k r)$, $T_{m,k}(\lambda_k r)$ and $Y_k(\lambda_k z)$ are defined by

$$S_{m,k}(\lambda_k r)=\frac{I_m(\lambda_k r)K_m(\lambda_k R_i)-I_m(\lambda_k R_i)K_m(\lambda_k r)}{I_m(\lambda_k R_e)K_m(\lambda_k R_i)-I_m(\lambda_k R_i)K_m(\lambda_k R_e)},\quad k>0; \tag{25a}$$

$$T_{m,k}(\lambda_k r)=\frac{I_m(\lambda_k R_e)K_m(\lambda_k r)-I_m(\lambda_k r)K_m(\lambda_k R_e)}{I_m(\lambda_k R_e)K_m(\lambda_k R_i)-I_m(\lambda_k R_i)K_m(\lambda_k R_e)},\quad k>0, \tag{25b}$$

and

$$Y_k(\lambda_k z)=\begin{cases}\dfrac{\sqrt{2}}{2}, & k=0,\\ \cos\left[\lambda_k(z+h)\right], & k\geq 1.\end{cases} \tag{26}$$

The limiting expressions of $S_{m,k}(\lambda_k r)$ and $T_{m,k}(\lambda_k r)$ as *m* and *l* approach 0 have been derived in Mavrakos (1985). That is

$$S_{m,k}(\lambda_k r)=\begin{cases}\dfrac{\ln(r/R_i)}{\ln(R_e/R_i)}, & m=0,\ k=0,\\ \dfrac{(r/R_i)^m-(R_i/r)^m}{(R_e/R_i)^m-(R_i/R_e)^m}, & m\neq 0,\ k=0;\end{cases} \tag{27a}$$

$$T_{m,k}(\lambda_k r)=\begin{cases}\dfrac{\ln(R_e/r)}{\ln(R_e/R_i)}, & m=0,\ k=0,\\ \dfrac{(R_e/r)^m-(r/R_e)^m}{(R_e/R_i)^m-(R_i/R_e)^m}, & m\neq 0,\ k=0.\end{cases} \tag{27b}$$

In Eqs. (25), (26) and (27), the eigenvalues λ_k are defined as $\lambda_k=k\pi/S$ to satisfy the boundary conditions on $z=-h$ and $z=-T$, in which $S=h-T$.

The infinite series in Eq. (15) representing the velocity potential is developed to satisfy Laplace's equation and all the boundary conditions except those at $r=R_i$ and $r=R_e$. In addition, the infinite series is truncated at an appropriate number to guarantee numerical convergence and accuracy. The unknown coefficients of the truncated eigenfunction series are determined by the continuity of the potential and its normal derivative across the three matching surfaces at $r=R_i$, $r=R_e$ and $r=R_b$.

The continuity condition of the velocity potential on the three matching surfaces provides the following three sets of linear equations:

$$\sum_{j=0}^{+\infty}\left(u_{j,\,l}A_{m,j}\right)-B_{m,\,l}=-J_m\left(\kappa_0 R_b\right)\sqrt{N_0}u_{0,\,l},\tag{28a}$$

$$\sum_{l=0}^{+\infty}\left(\frac{2}{S}v_{l,\,k}C_{m,\,l}\right)-D_{m,\,k}=0;\tag{28b}$$

$$E_{m,\,k}-\sum_{j=0}^{+\infty}\left(\frac{2}{S}w_{j,\,k}F_{m,j}\right)=\begin{cases}-\dfrac{2\sqrt{2}\mathrm{i}\pi\omega\Lambda}{\rho g}\displaystyle\sum_{j=0}^{+\infty}\left(\frac{F_{0,j}}{\sqrt{N_j}}\Pi_j\right), & m=k=0,\\ 0, & m\neq 0 \text{ or } k\neq 0.\end{cases}\tag{28c}$$

Furthermore, the continuity condition of the normal derivative of the velocity potential on the three matching surfaces provides another three sets of linear equations:

$$A_{m,j}-\sum_{l=0}^{+\infty}\left\{\frac{\mu_l\left[B_{m,\,l}P'_{m,\,l}\left(\mu_l R_b\right)+C_{m,\,l}Q'_{m,\,l}\left(\mu_l R_b\right)\right]}{\kappa_j R'_{m,j}\left(\kappa_j R_b\right)}u_{jl}\right\}=\begin{cases}-\dfrac{J'_m\left(\kappa_0 R_b\right)}{R'_{m,j}\left(\kappa_j R_b\right)}\sqrt{N_0}, & j=0,\\ 0, & j\neq 0,\end{cases}\tag{29a}$$

$$B_{m,\,l}\frac{P'_{m,\,l}\left(\mu_l R_e\right)}{Q'_{m,\,l}\left(\mu_l R_e\right)}+C_{m,\,l}-\sum_{k=0}^{+\infty}\left\{\frac{\lambda_k v_{l,\,k}\left[S'_{m,\,k}\left(\lambda_k R_e\right)D_{m,\,k}+T'_{m,\,k}\left(\lambda_k R_e\right)E_{m,\,k}\right]}{\mu_l Q'_{m,\,l}\left(\mu_l R_e\right)}\right\}=0,\tag{29b}$$

$$\sum_{k=0}^{+\infty}\left\{\frac{\lambda_k w_{j,\,k}\left[D_{m,\,k}S'_{m,\,k}\left(\lambda_k R_i\right)+E_{m,\,k}T'_{m,\,k}\left(\lambda_k R_i\right)\right]}{\kappa_j W'_{m,j}\left(\kappa_j R_i\right)U_j\left(\kappa_j h\right)}\right\}-F_{m,j}=0.\tag{29c}$$

In Eq. (29), the prime in the superscript denotes the derivative with respect to the argument. In Eqs. (28) and (29), the coefficients $u_{j,\,l}$, $v_{l,\,k}$ and $w_{j,\,k}$ are defined by

$$u_{j,\,l}=\int_{-h}^{0}Z_j\left(\kappa_j z\right)U_l\left(\mu_l z\right)\mathrm{d}z;\tag{30a}$$

$$v_{l,\,k}=\int_{-h}^{-T}U_l\left(\mu_l z\right)Y_k\left(\lambda_k z\right)\mathrm{d}z;\tag{30b}$$

$$w_{j,\,k}=\int_{-h}^{-T}Z_j\left(\kappa_j z\right)Y_k\left(\lambda_k z\right)\mathrm{d}z.\tag{30c}$$

Now six sets of linear systems with an equal number of unknowns have been set up. It is noted that the diagonal submatrices of the linear system are all units due to the orthogonality of the vertical eigenfunctions, which makes the linear system better suited to numerical solutions. Solving the equations gives the unknown coefficients in the orthogonal series and the velocity potentials valid in each subdomain.

Once the solution for the velocity potential is known, the other physical quantities of interest can be immediately obtained. Based on the kinematic conditions on the free surface, the wave elevation amplitude η can be expressed as

$$\eta = -\frac{1}{\mathrm{i}\omega}\frac{\partial\phi}{\partial z}\bigg|_{z=0}. \tag{31}$$

After expanding the wave elevation into the Fourier-cosine series in the circumferential direction, the wave elevation can be expressed as a summation of contributions from different orders. That is

$$\eta = \sum_{m=0}^{+\infty}\eta_m = A\sum_{m=0}^{+\infty}\left(\varepsilon_m \mathrm{i}^m \psi_m \cos m\theta\right), \tag{32}$$

where A is the incident wave amplitude; η_m is the mth order Fourier component of the wave elevation. The expression of ψ_m is given by

$$\psi_m = \begin{cases} J_m(\kappa_0 r) + \sum\limits_{j=0}^{+\infty}\left[\dfrac{1}{\sqrt{N_j}}A_{m,j}R_{m,j}(\kappa_j r)\right], & \text{in } \Omega_1, \\ \sum\limits_{l=0}^{+\infty}\left\{\dfrac{1}{\sqrt{M_l}}\left[B_{m,l}P_{m,l}(\mu_l r) + C_{m,l}Q_{m,l}(\mu_l r)\right]\right\}, & \text{in } \Omega_2, \\ \sum\limits_{j=0}^{+\infty}\left[\dfrac{1}{\sqrt{N_j}}F_{m,j}W_{m,j}(\kappa_j r)\right], & \text{in } \Omega_4. \end{cases} \tag{33}$$

The air volume flux through the air turbine can be obtained by integrating the vertical fluid velocity over S_i. The complex amplitude of the air volume flux can be expressed as

$$q_c = -2\mathrm{i}A\omega\pi\sum_{j=0}^{+\infty}\left(\frac{F_{0,j}}{\sqrt{N_j}}\Pi_j\right). \tag{34}$$

The definition of Π_j has been given in Eq. (20). After getting the air volume flux, the oscillating air pressure in the chamber and the captured wave power can be determined according to Eqs. (10) and (14), respectively.

In addition, the hydrodynamic wave loading can be determined through a pressure integration over the wetted body surface. By considering linear harmonic incident wave, the time factor can be separated, and the wave force and moment can be expressed as

$$F_x(t) = \mathrm{Re}\left[f_x e^{-\mathrm{i}\omega t}\right], \tag{35a}$$

$$F_z(t) = \mathrm{Re}\left[f_z e^{-\mathrm{i}\omega t} \right], \tag{35b}$$

$$M_y(t) = \mathrm{Re}\left[m_y e^{-\mathrm{i}\omega t} \right], \tag{35c}$$

where F_x, F_z and M_y are the horizontal wave force, vertical wave force, and the wave moment around the y-axis; f_x, f_z and m_y are the complex amplitudes.

The detailed expressions of the horizontal and vertical wave force amplitude, denoted by f_x and f_z, respectively, are given by:

$$f_x = 2\mathrm{i}A\rho g\pi \cdot \left\{ -R_e \sum_{l=0}^{+\infty} \left(C_{1,l} I_{z,l}^1 \right) + R_i \sum_{j=0}^{+\infty} \left(F_{1,j} I_{z,j}^2 \right) - a \sum_{j=0}^{+\infty} \left[F_{1,j} W_{1,j}\left(\kappa_j a \right) I_{z,j}^3 \right] \right\}, \tag{36a}$$

$$\begin{aligned} f_z = 2A\rho g\pi \cdot & \left\{ \sum_{l=0}^{+\infty} \left[\frac{U_l'(-\mu_l d)}{\mu_l} \cdot \left(B_{0,l} I_{r,l}^1(R_b) + C_{0,l} I_{r,l}^2(R_b) - B_{0,l} I_{r,l}^1(R_e) - C_{0,l} I_{r,l}^2(R_e) \right) \right] \right. \\ & \left. + \sum_{k=0}^{+\infty} \left[Y_k(-\lambda_k T) \cdot \left(D_{0,k} I_{r,k}^3(R_e) + E_{0,k} I_{r,k}^4(R_e) - D_{0,k} I_{r,k}^3(R_i) - E_{0,k} I_{r,k}^4(R_i) \right) \right] \right\}, \end{aligned} \tag{36b}$$

where the coefficients $I_{z,l}^1$, $I_{z,j}^2$ and $I_{z,j}^3$ as well as the functions $I_{r,l}^1(r)$, $I_{r,l}^2(r)$, $I_{r,k}^3(r)$ and $I_{r,k}^4(r)$ are defined in Appendix B. The detailed expression of the wave moment m_y can be derived similarly to the wave force and hence not shown here for brevity.

5. Numerical computation and analysis

5.1 Convergence test and validation

Numerical computation is then conducted using the developed model. In the computation, we use $\rho = 1.025\times10^3$ kg/m^3, $\rho_a = 1.293$ kg/m^3, $g = 9.807$ m/s^2 and $c = 340$ m/s, respectively. The convergence of the present model is examined to ensure that the present results are free from the influence of the truncation number. The number of eigenmodes can affect the computational accuracy of the wave energy harvesting and the wave force/moment. The variation of W_c, f_x, f_z and m_y with different numbers of eigenmodes is shown in Fig. 3. It can be seen that the results based on 50, 150 and 200 eigenmodes are in good consistency. Regarding the computation of the free-surface elevation, not only the number of eigenmodes but also that of Fourier modes can affect the accuracy. Table. 1 presents the dimensionless wave elevation amplitude at three specific locations P_1, P_2 and P_3, respectively, with different numbers of Fourier modes. In the cylindrical system, the horizontal coordinates of P_1, P_2 and P_3 are $((a + R_e)/2, 0)$, $((a + R_e)/2, \pi/6)$ and $((a + R_e)/2, \pi/3)$, respectively. Hereinafter, the incident wave amplitude A is used to nondimensionalize the free-surface elevation amplitude. It is noted that excellent convergence can be achieved when 10 Fourier modes are used. From Fig. 3 and Table 1, it can be seen that the convergence is satisfactory. 100 eigen modes and 10 Fourier modes are sufficient to guarantee satisfactory accuracy. Therefore, they are adopted in all the subsequent computations.

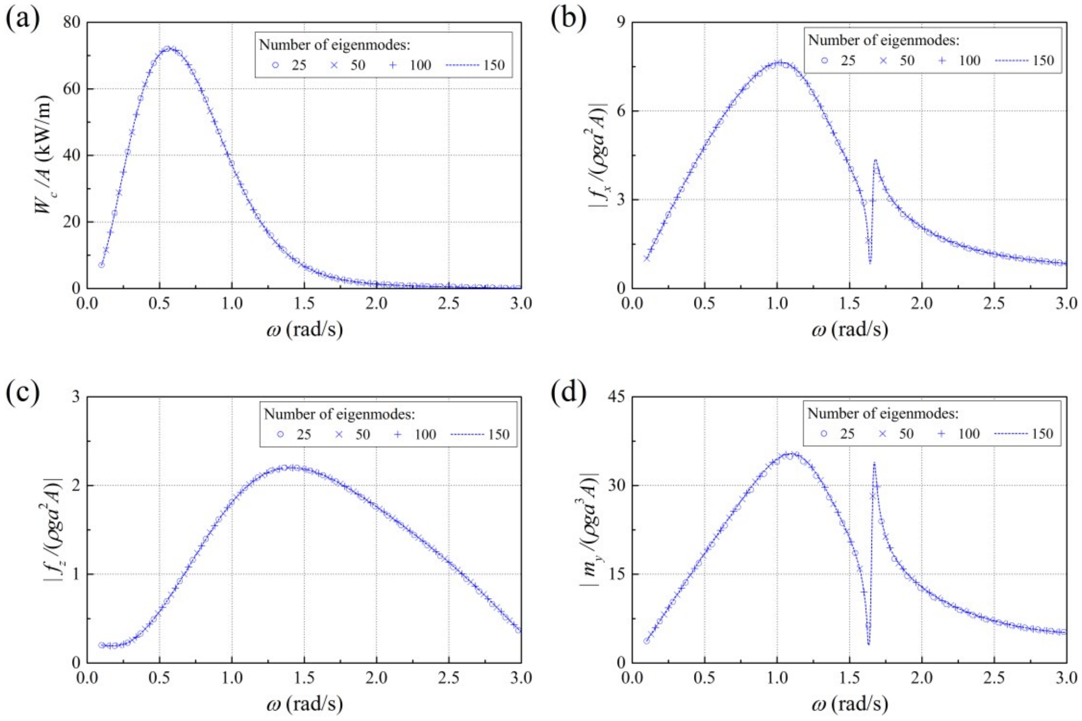

Fig. 3. Comparison of the computational results with respect to the number of eigenmodes for a hybrid system with $a = 3$ m, $R_i = 5.95$ m, $R_i = 6.0$ m, $d = 1.0$ m, $T = 3.0$ m and $\sigma = 0.5$ m^{-1} in water of depth $h = 20$ m. The parameters associated with the air chamber and air turbine are $K = 0.45$, $D = 2.0$ m, $h_0 = 3.0$ m and $N = 150$ rpm. The results are presented for (a) W_c, (b) f_x, (c) f_z and (d) m_y.

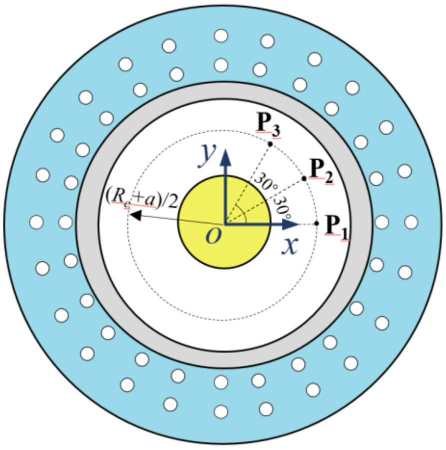

Fig. 4 Plane view of the locations of P_1, P_2, and P_3.

Table 1. Variation of the computational results of free-surface elevation with respect to the number of Fourier modes. The parameters associated with the hybrid system, air chamber and air turbine used in the computation are the same as those for Fig. 3. Besides, 100 eigenmodes are used. The results are presented for ω = 0.6 rad/s (left column), 1.2 rad/s (middle column) and 1.8 rad/s (right column).

Number of Fourier modes	Nondimensionalized free-surface elevation $\lvert\eta/A\rvert$ at P_1, P_2 and P_3								
	P_1			P_2			P_3		
1	0.7044	0.6792	0.6130	0.6738	0.5944	0.3816	0.5156	0.4467	0.2591
2	0.7013	0.6776	0.6148	0.6748	0.5939	0.3863	0.5974	0.4865	0.2256
5	0.7013	0.6776	0.6149	0.6725	0.5939	0.3886	0.6042	0.4872	0.2140
10	0.7013	0.6776	0.6149	0.6725	0.5939	0.3886	0.6042	0.4872	0.2140
15	0.7013	0.6776	0.6149	0.6725	0.5939	0.3886	0.6042	0.4872	0.2140

To further verify, the wave force and moment on a vertical cylinder with a submerged porous plate are computed, and the results are compared with those published by Li et al. (2022c). The potential decomposition method was used by Li et al. (2022c). In the present computation, the chamber's width and the plate's thickness are set as 0.001 m. The excellent agreement in Fig. 5 further verifies the validity of the present model.

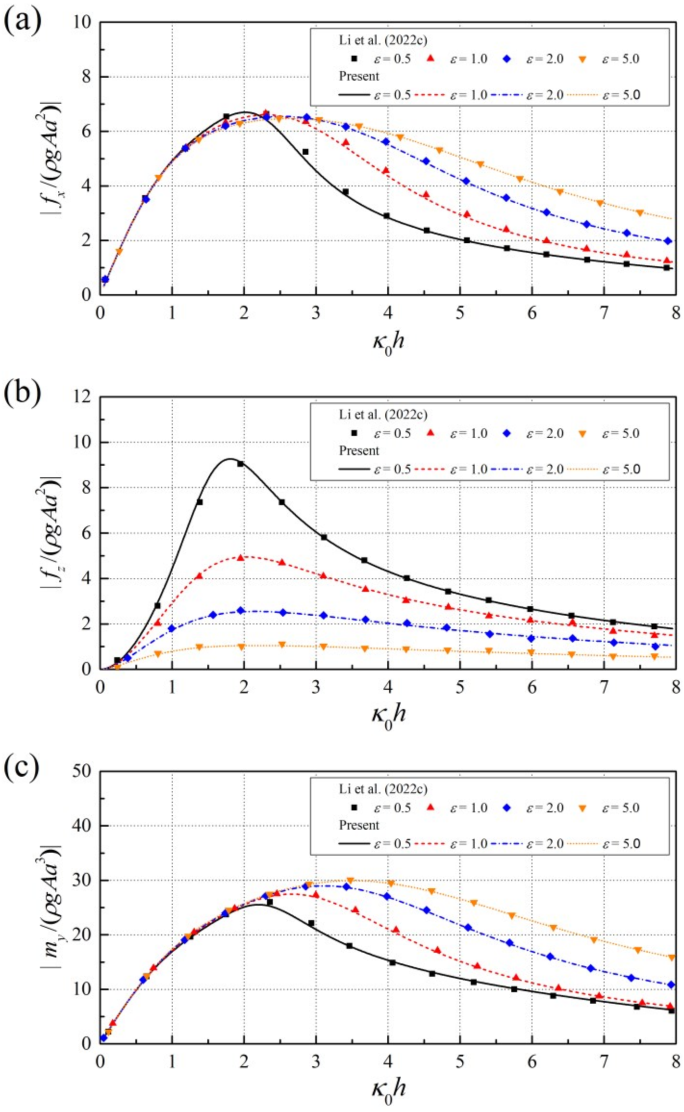

Fig. 5 Comparison of the wave force and moment on a vertical cylinder with a submerged perforated plate for different porous-effect parameters (σ), where $\sigma = \kappa_0\varepsilon(1+\mathrm{i})$. Geometrical parameters are $a/h = 0.15$, $R_b/h = 0.3$ and $d/h = 0.0125$. The symbols and lines represent the present results and Li et al. (2022c)'s results, respectively: (a) f_x, (b) f_z and (c) m_y.

5.2 Results and Discussion

Numerical studies are conducted in detail in this section. The numerical results are in full scale unless otherwise stated. They are first presented for regular sea conditions and then extended to irregular conditions. In the subsequent computation, the water depth is $h = 20$ m. In addition, the radius of the monopile foundation $a = 3$ m. The draft of the air chamber is $T = 3.0$ m, the exterior radius of the chamber is $R_e = 6.0$ m, and the thickness of the exterior shell is $R_e - R_i = 0.05$ m. Meanwhile, $K = 0.45$, $D = 2.0$ m and $h_0 = 3.0$ m are used for the turbine and chamber parameters.

5.2.1 Determination of the Turbine Rotational Speed

The effect of the rotational speed of the air turbine on wave energy harvesting is first discussed. Computation is conducted for the case that the horizontal perforated plate is removed from the system, i.e., $\sigma = +\infty$. The rotational speed of the air turbine varies from 5 rpm to 1000 rpm. In addition, incident waves of unit amplitude are used, and the wave frequencies cover a wide range.

From Fig. 6, it is noted that an optimal rotational speed exists for each wave frequency. The optimal rotational speed shift towards the low-speed region with the increase of wave frequency. The annual-shaped OWC can bring about significant wave energy harvesting, especially when $N \leq 200$ rpm. As a slow speed is unrealistic in practice, $N = 150$ rpm is used for the subsequent computation. When $N = 150$ rpm, the most pronounced energy harvesting is around $\omega = 0.58$ rad/s, within the frequency range of significant ocean waves.

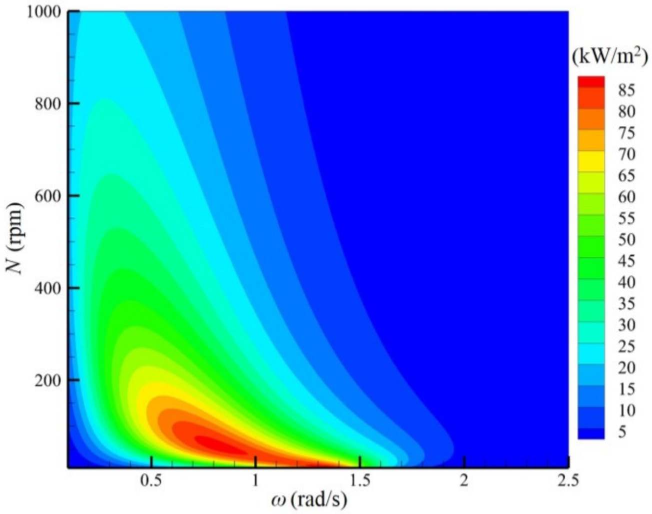

Fig. 6 Variation of the wave energy harvesting with respect to the combination of (ω, N) for unit incident wave amplitude without the perforated plate.

5.2.2 Air volume flux and oscillating air pressure

Effects of the porosity, size and submergence depth of the attached plate on the air volume flux and oscillating air pressure are shown in Figs. 7~9, respectively. For comparison, the results for the cases without the perforated plate are also added to these figures and denoted by 'W/O plate'. The oscillating air pressure p_c can be related to the air volume flux q_c through the pneumatic damping coefficient Λ. The real part of Λ depends on the design of the air turbine and does not change with the wave frequency. In contrast, the imaginary part of Λ is analogous to the air spring force caused by the compressibility of air in the chamber. When the air volume in the chamber is not large, the air spring force plays a secondary role, and Λ is dominated by its real part. Consequently, in Figs. 7~9, the oscillating air pressure almost linearly depends on the air volume flux over the whole frequency region.

In Fig. 7, for long incident waves, the oscillating air pressure and air volume flux grow gradually with the increase of σ. This can be explained by the fact that when the porous-effect parameter σ grows progressively and tends to infinity, the attached plate gradually loses its ability to dissipate the incident wave energy and tends to be transparent (i.e., the plate is removed). Then, more wave energy is available to the OWC, which leads to more apparent oscillation of the interior free surface. In Fig. 7, it can also be noted that for short incident waves, a decrease of σ can give rise to an increase of p_c and q_c. This is because when σ tends to zero, the attached plate gradually turns into a rigid one, and its effects in reflecting the incident waves become significant. In some conditions, this can cause wave trapping in the vicinity of the plate and, in turn, enhance the free-surface oscillation in the chamber. A larger plate can attenuate the wave energy over a broader fluid region. Meanwhile, as the velocity of the fluid particle decays exponentially along the vertical direction, a plate of lower submergence depth is more effective in dissipating incident wave energy. As a result, in Figs. 8 and 9, p_c and q_c decay gradually with the increase of b or the decrease of d.

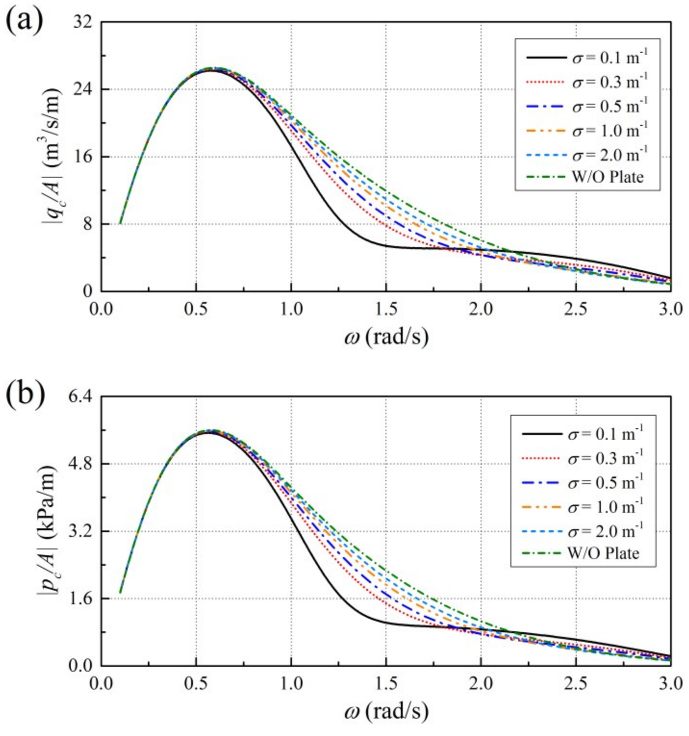

Fig. 7 Variation of the air volume flux (q_c) and oscillating air pressure (p_c) with different porous-effect parameters for b = 3.0 m, d = 1.0 m and N = 150 rpm: (a) q_c and (b) p_c.

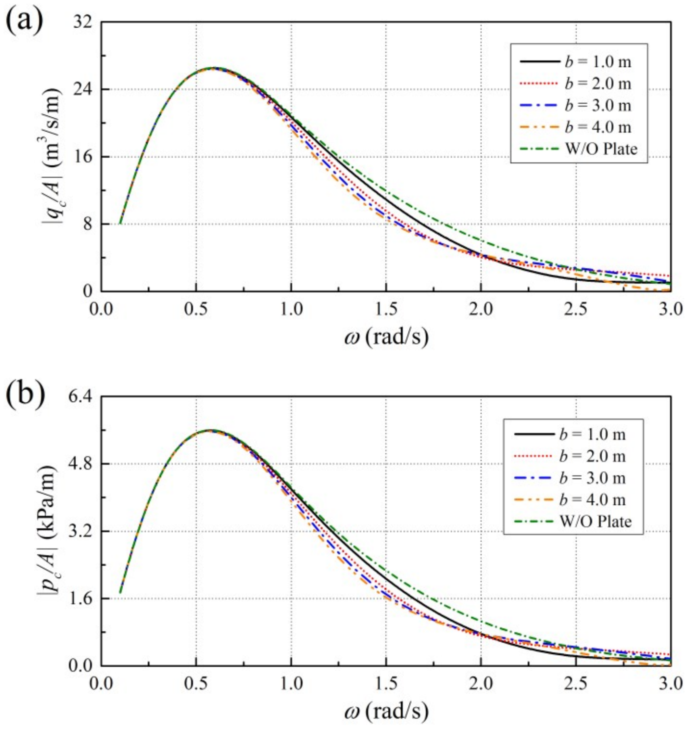

Fig. 8 Variation of the air volume flux (q_c) and oscillating air pressure (p_c) with different plate widths for σ = 0.5 m^{-1}, d = 1.0 m and N = 150 rpm: (a) q_c and (b) p_c.

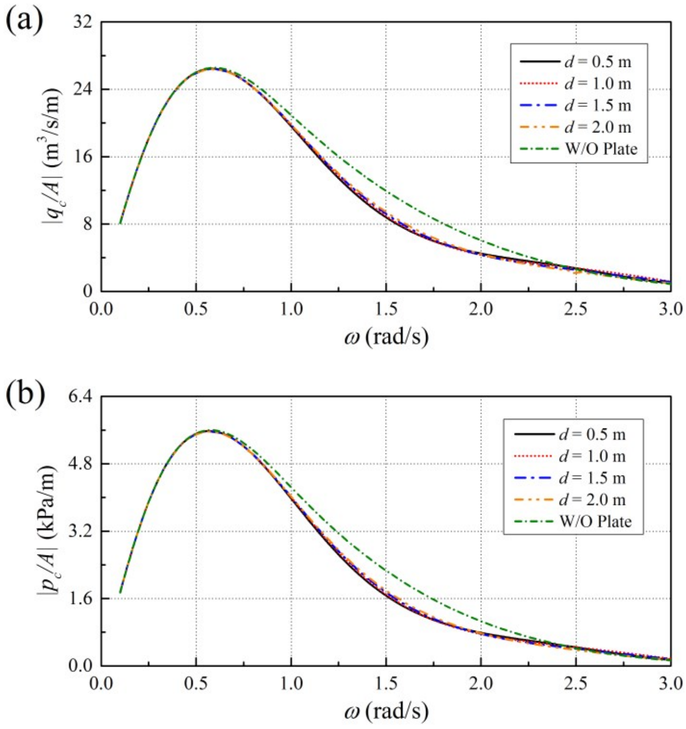

Fig. 9 Variation of the air volume flux (q_c) and oscillating air pressure (p_c) with different plate drafts for $\sigma = 0.5$ m^{-1}, $b = 3.0$ m and $N = 150$ rpm: (a) q_c and (b) p_c.

5.2.3 Wave energy harvesting

Effects of the porosity, size and submergence depth of the attached plate on the wave energy harvesting of the OWC are shown in Figs. 10~12, respectively. The wave energy harvesting follows a similar trend as the air volume flux or oscillating air pressure. When the wavelength is significantly longer compared with the characteristic size of the system, the wave diffraction by the system is negligible, and the interior free surface experiences almost no disturbance. With the increase of the wave frequency, the wave diffraction effect becomes noticeable, motivating the oscillation of the interior free surface. Consequently, in the low-frequency region, the wave energy harvesting continues to increase as the wave frequency increases until it reaches the dominant peak. As the wave frequency increases further, the exterior shell of the OWC imposes an apparat shielding effect on the interior free surface, which prevents the incident waves from travelling inside the interior region. As a result, the wave energy harvesting decays gradually as the wave frequency increases further after it reaches the dominant peak. Similar to the air volume flux and the oscillating air pressure, a smaller porous-effect parameter, a larger plate size, or a shallower submergence depth gives rise to a lower wave energy harvesting and shrinks the frequency region of high wave energy harvesting.

The porosity, size and submergence depth of the attached plate imposes negligible effect on the peak frequency of wave energy harvesting. It is also noted that the impact of the perforated plate on wave energy harvesting is much less noticeable in the low-frequency region than in the high-frequency region. This can be attributed to the fact that long waves can better pass through porous media.

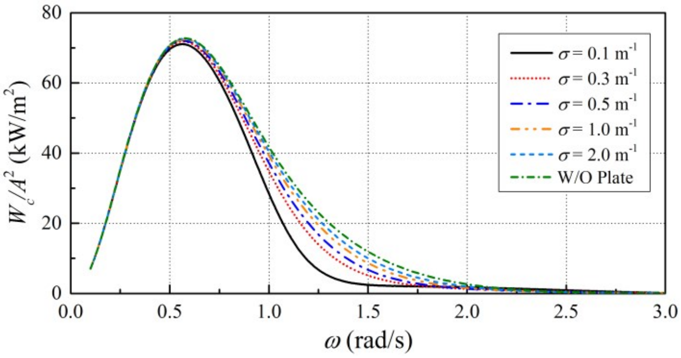

Fig. 10 Variation of the wave energy harvesting with different porous-effect parameters (σ) for b = 3.0 m, d = 1.0 m and N = 150 rpm.

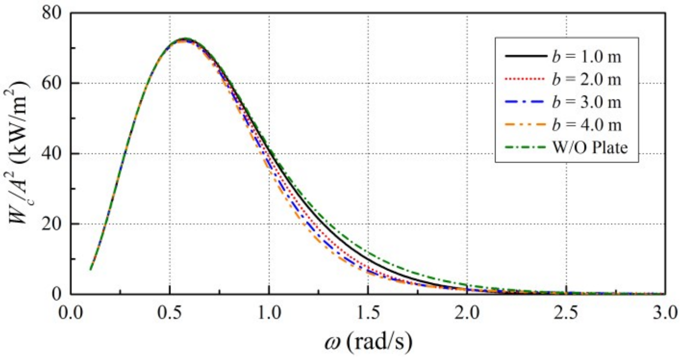

Fig. 11 Variation of the wave energy harvesting with different plate widths (b) for σ = 0.5 m^{-1}, d = 1.0 m and N = 150 rpm.

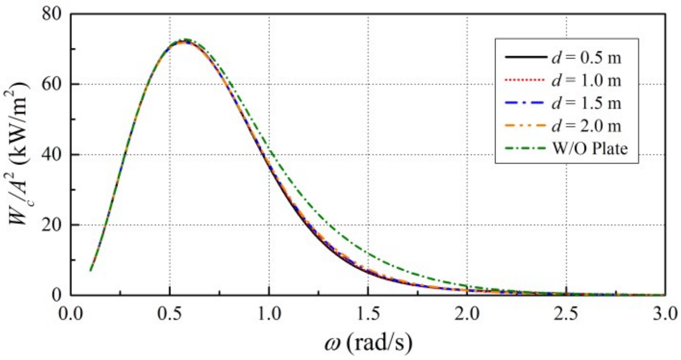

Fig. 12 Variation of the wave energy harvesting with different plate drafts (d) for $\sigma = 0.5$ m^{-1}, b = 3.0 m and N = 150 rpm.

5.2.4 Wave force and moment on the combined system

Offshore foundations are subjected to the cyclic loads generated by environmental conditions. In the ocean environment, hydrodynamics is a primary source of variable loads. In geotechnical design, the importance of loading type depends on the foundation system. For monopile foundations, the vertical wave force is much smaller than the self-weight of the foundation. The lateral wave force, which can cause the monopile's lateral deflection (rotation), is more critical and controls the serviceability limit state of the whole structure (Arshad and O'Kelly, 2016).

The wave force and moment are shown in Fig. 13 for different porous-effect parameters. In these figures, the results denoted by 'SC' correspond to the case of a single monopile, i.e., the OWC is removed from the hybrid system. The effects of the porosity on the horizontal wave force (see Fig. 13(a)) are first discussed. The horizontal wave force on a monopile is characterized by one single peak. However, when an OWC is added to the system, the wave force (denoted by 'W/O plate') has two noticeable peaks. A specific wave frequency exists between the two peaks at which the wave forces on the OWC and the monopile can balance each other, leading to a nearly zero net force on the system. While in the remaining wave frequency region, the presence of the OWC gives rise to the additional wave force. When the perforated plate is used, the wave force on the system (denoted by '$\sigma = 0.1$ m^{-1}, 0.3 m^{-1}, …, and 2.0 m^{-1}') is lower than without the plate and generally decays with the decrease of σ. This is because wave energy dissipation can remit the wave impact with the system. An exception is found around the first peak when $\sigma = 0.1\ \mathrm{m}^{-1}$. This can be attributed to the fact that when the porosity of the plate is quite low, the wave reflection by the plate is remarkable. This can lead to apparent wave energy focusing in the vicinity of the plate at specific conditions and reinforce the wave force on the system. It is also noted that when σ is lower than $0.5\ \mathrm{m}^{-1}$, there exists a particular frequency beyond which the wave force on the hybrid system is lower than that on a monopile. This frequency moves gradually to the low-frequency region as σ decreases. The vertical force (see Fig. 13(b)) grows gradually with the decrease of σ. This is because, for a plate with higher porosity, the fluid particle can travel through the plate more efficiently, which weakens the wave action with the plate. The wave moment on the system (see Fig. 13(c)) follows a similar trend as that of the horizontal wave force. It is noted that for the horizontal wave force and wave moment, the frequencies of the two peaks are larger than that of the wave energy harvesting. It suggests that reducing the wave force of short waves is more critical.

The plate width and submergence depth effects on the wave force and moment are shown in Figs. 14~15. The wave diffraction process can affect a wide region of wave field around the system. Meanwhile, the wave energy is concentrated along the vertical direction near the free surface. It suggests that a plate of a larger width and shallower submergence depth can better protect the system. At the same time, it experiences a stronger wave action. As a result, the horizontal wave force and moment decay gradually with the increase of plate width or the decrease of submergence depth. At the same time, the vertical wave force follows a reversed trend.

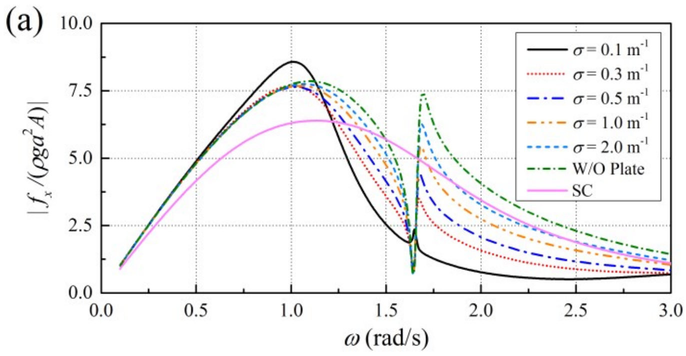

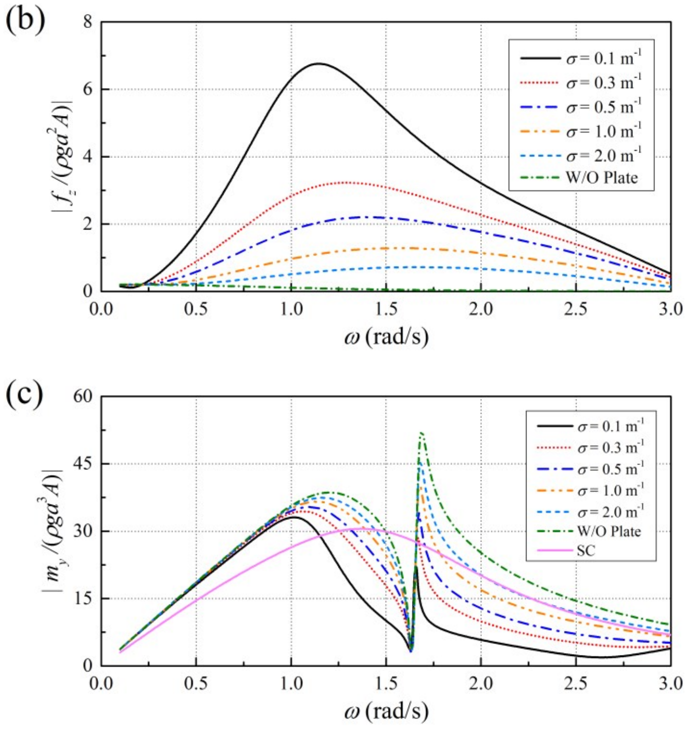

Fig. 13 Variation of the wave force and moment with different porous-effect parameters (σ) for b = 3.0 m and d = 1.0 m: (a) f_x, (b) f_z and (c) m_y

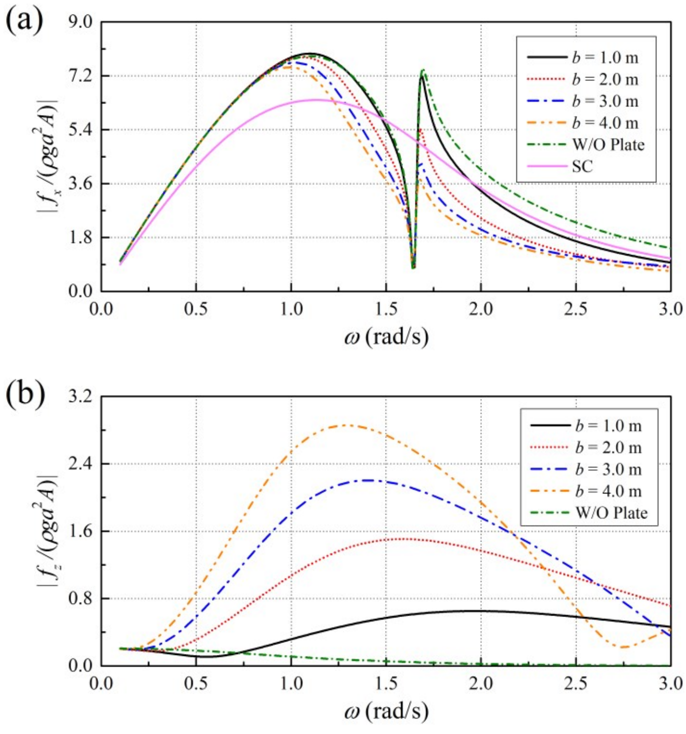

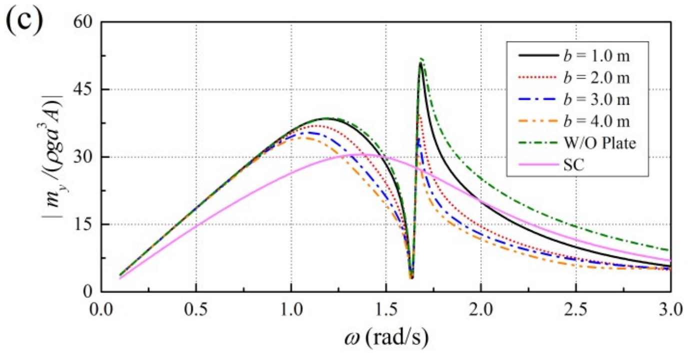

Fig. 14 Variation of the wave force and moment with different plate widths (b) for $\sigma = 0.5$ m^{-1} and $d = 1.0$ m: (a) f_x, (b) f_z and (c) m_y

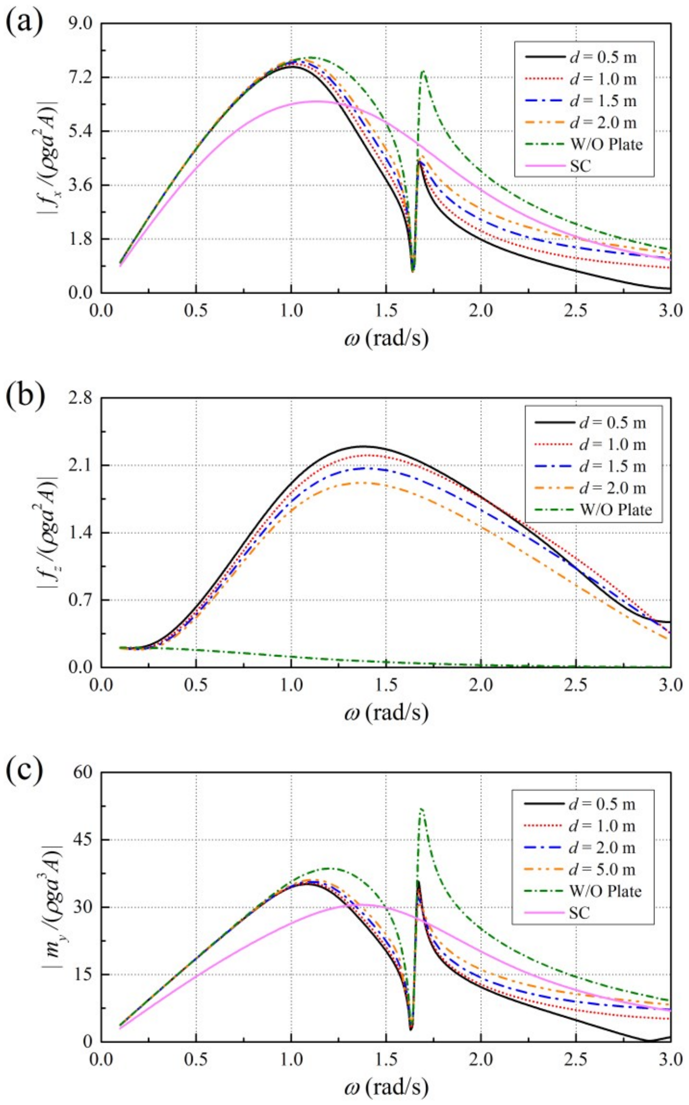

Fig. 15 Variation of the wave force and moment with different plate drafts (d) for $\sigma = 0.5$ m^{-1} and $b = 3.0$ m: (a) f_x, (b) f_z and (c) m_y

5.2.5 Free-surface oscillation in the vicinity of the system

The free-surface oscillation in the vicinity of the system is considered. In Fig. 16, the variation of the free-surface elevation amplitude at P$_1$, P$_2$ and P$_3$ is plotted with different porous-effect parameters. Three noticeable peaks are attained around ω = 1.67 rad/s, 2.14 rad/s, and 2.56 rad/s, respectively, associated with varying modes of resonant wave motion within the chamber. It is also noted that the use of the perforated plate is effective in suppressing the resonant response. The free-surface elevation at a specific location can be expanded into Fourier series with respect to the circumferential coordinate θ (see Eq. (32)). The variation of different Fourier components of the free-surface elevation at P$_1$, P$_2$ and P$_3$ is shown in Fig. 17. It is found that the 1st, 2nd and 3rd order Fourier components, respectively contribute the three prominent peaks of the overall free-surface elevation. The wave frequencies corresponding to these peaks are $\omega_{p=1}$, $\omega_{p=2}$ and $\omega_{p=3}$, hereinafter. The remarkable peak at $\omega_{p=3}$ vanishes at the location of P$_3$. This is caused by the fact that P$_3$ is at the nodal point of the p = 3 resonance mode. Due to the air chamber's symmetry and the uniform air pressure distribution over the interior free surface, the air pressure can only affect the Fourier component with no variation in the circumferential direction, i.e., the 0th-order component. The resonance frequency of the p = 0 mode, around ω = 1.39 rad/s, is defined as $\omega_{p=0}$, hereinafter. Therefore, in Figs. 16~17, the noticeable amplification of the free-surface elevation at $\omega_{p=0}$ cannot be found.

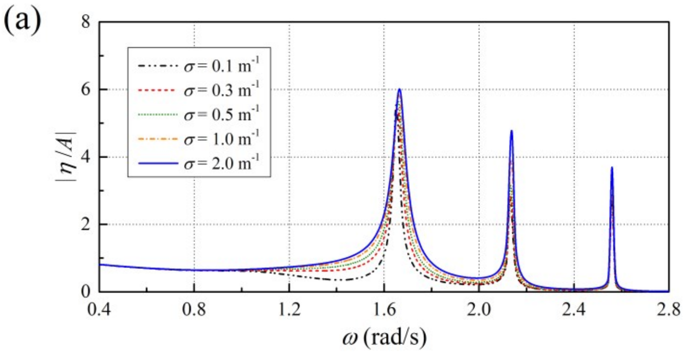

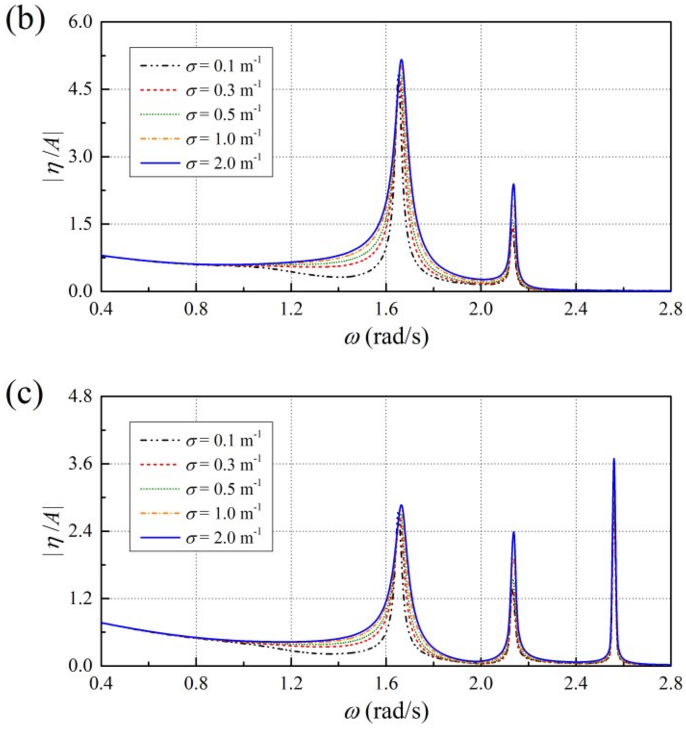

Fig. 16 Free-surface elevation amplitude at P_1, P_2 and P_3 with d = 1.0 m, b = 3.0 m and N = 150 rpm: (a) P_1, (b) P_2 and (c) P_3

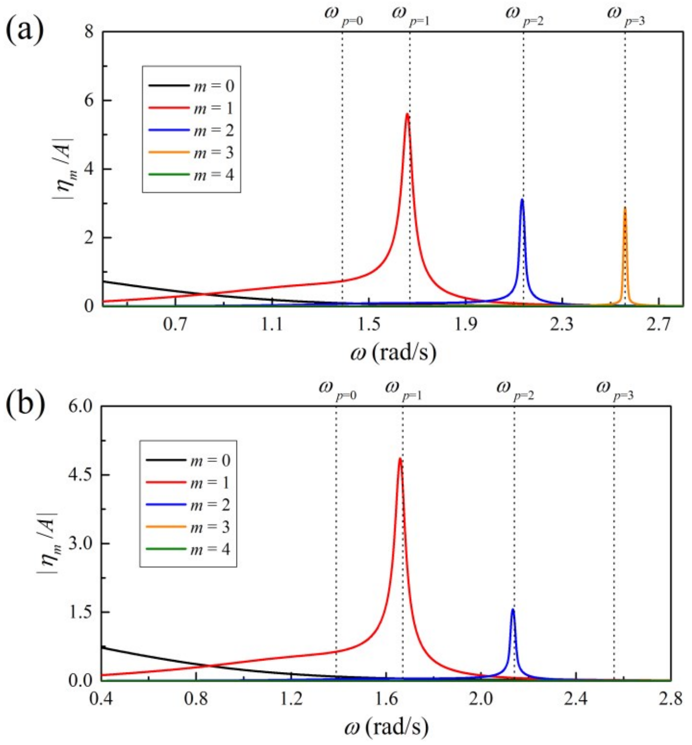

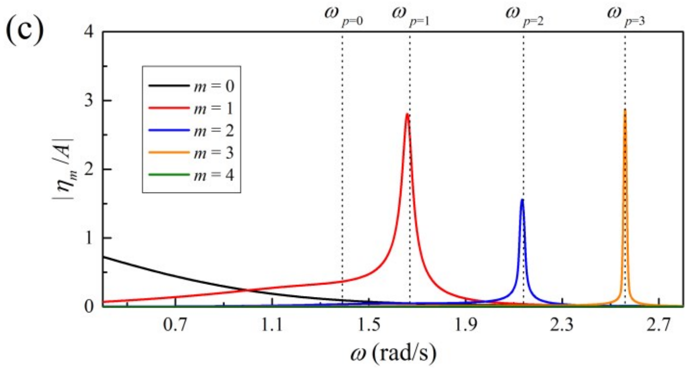

Fig. 17 Fourier components of the free-surface elevation amplitude at P$_1$, P$_2$ and P$_3$ with $\sigma = 0.5$ m^{-1}, $d = 1.0$ m, $b = 3.0$ m and $N = 150$ rpm: (a) P$_1$, (b) P$_2$ and (c) P$_3$

The distribution of the free-surface elevation amplitude in the vicinity of the system is shown in Fig. 18 for $\omega_{p=1}$, $\omega_{p=2}$ and $\omega_{p=3}$, respectively. To further emphasize the characteristics of the free-surface oscillation inside the chamber, the wave runup along $r = a$ and $r = R_i$ are shown in Fig. 19 for these wave frequencies. It is noted that the free-surface elevation has periodic variation along the circumferential direction inside the chamber. Antisymmetric modes of the free-surface oscillation about $\theta = (1/2 + n)\pi$, $(1/4 + n/2)\pi$ and $(1/6 + n/3)\pi$, in which $n = 0, 1, 2, \ldots$, can be observed for the $p = 1$, 2 and 3 modes, respectively. When a significant peak is attained at a specific location, a trough with nearly the same magnitude can simultaneously appear in a neighbouring region. Consequently, its overall contribution to the air volume flux and wave power harvesting is not considerable.

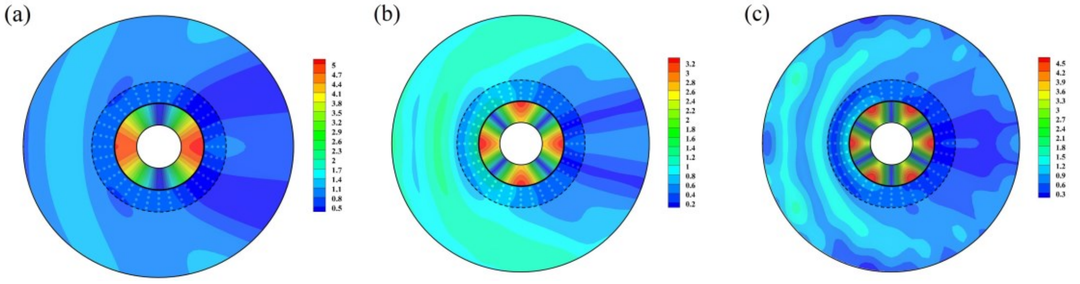

Fig. 18 Dimensionless free-surface elevation amplitude $|\eta/A|$ in the vicinity of the system at specific wave frequencies with $\sigma = 0.5$ m^{-1}, $d = 1.0$ m, $b = 3.0$ m and $N = 150$ rpm: (a) $\omega_{p=1}$, (b) $\omega_{p=2}$ and (c) $\omega_{p=3}$.

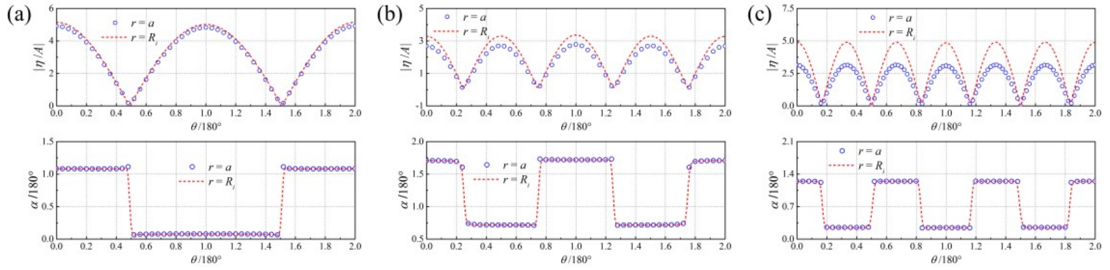

Fig. 19 Magnitude and phase angle of wave runup along $r = a$ and $r = R_i$ at specific wave frequencies with $\sigma = 0.5$ m^{-1}, $d = 1.0$ m, $b = 3.0$ m and $N = 150$ rpm: (a) $\omega_{p=1}$, (b) $\omega_{p=2}$ and (c) $\omega_{p=3}$.

The piston mode of resonant wave motion inside the chamber is then discussed. The distribution of the free-surface elevation amplitude around the system is shown in Fig. 20 for $\omega_{p=0}$. The corresponding wave runups along $r = a$ and $r = R_i$ are demonstrated in Fig. 21. When the PTO system is removed, i.e., $N = 0$, the interior free surface is subjected to constant atmospheric pressure. In this case, the free-surface elevation experiences no apparent variation in both the radial and circumferential directions, and the fluid inside the chamber behaves like a rigid body (see Figs. 20(a) and 21(a)). In addition, the use of the perforated plate leads to a slight decrease in the wave runup (see Fig. 20(b) and 21(b)). When the PTO system is installed, oscillating air pressure is applied on the interior free surface. Due to its influence, the 0th-order Fourier component of the free-surface elevation, which contributes to the piston-mode wave motion, gets weakened. In contrast, other components can impose more and more significant disturbance on the overall elevation. Then, the free-surface elevation inside the chamber loses its uniform distribution (see Figs. 20(c) and 21(c)) and varies apparently along the circumferential direction, leading to a breakdown of the piston-mode resonance.

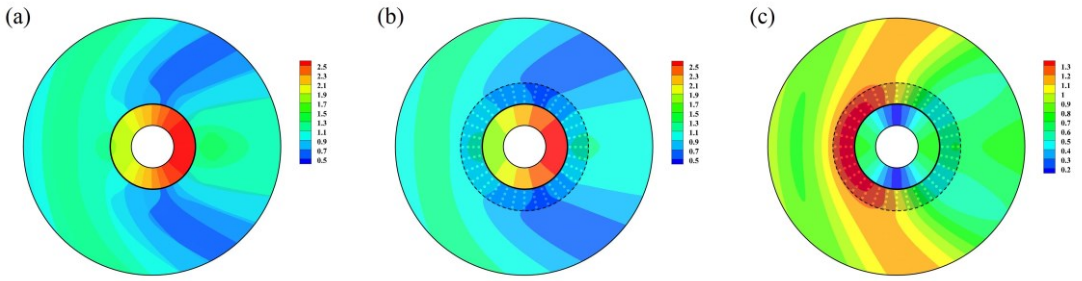

Fig. 20 Dimensionless free-surface elevation amplitude $|\eta/A|$ in the vicinity of the system at $\omega_{p=0}$ with $d = 1.0$ m and $b = 3.0$ m: (a) $(\sigma, N) = (+\infty, 0)$, (b) $(\sigma, N) = (0.5$ m$^{-1}, 0)$ and (c) $(\sigma, N) = (0.5$ m^{-1},

150 rpm).

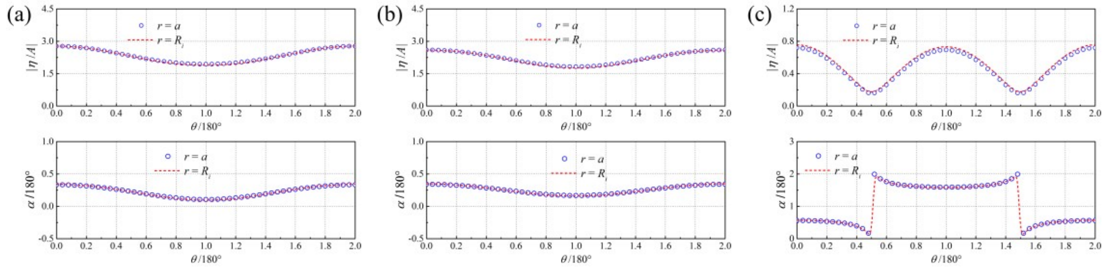

Fig. 21 Magnitude and phase angle of wave runup along $r = a$ and $r = R_i$ at $\omega_{p=0}$ with $d = 1.0$ m and $b = 3.0$ m: (a) $(\sigma, N) = (+\infty, 0)$, (b) $(\sigma, N) = (0.5\ \mathrm{m}^{-1}, 0)$ and (c) $(\sigma, N) = (0.5\ \mathrm{m}^{-1}, 150\ \mathrm{rpm})$.

5.2.6 Extension to the irregular sea conditions

The investigation is extended to irregular sea conditions. An irregular wave train can be regarded as the superposition of large numbers of linear harmonic wave components with different wave heights, angular frequencies and initial phases. The wave height of the jth wave component is determined by

$$H_j = 2\sqrt{2S\left(\omega_j\right)\Delta\omega}, \quad j = 1,\ 2,\ \ldots \tag{37}$$

in which $S(\omega)$ is the spectral density function. When the wave spectrum is divided into J parts, and the frequency bandwidth $\Delta\omega$ keeps the same in each part, we can have

$$\Delta\omega = \frac{\omega_H - \omega_L}{J}; \tag{38a}$$

$$\omega_j = \omega_L + (j - 0.5)\Delta\omega, \quad j = 1,\ 2,\ \ldots \tag{38b}$$

in which ω_H and ω_L are high and low cut-off frequencies, respectively. In this study, $\omega_L = 0.05$ rad/s, $\omega_H = 2.95$ rad/s and $\Delta\omega = 0.01$ rad/s are used to simulate the incident waves. In addition, in irregular sea conditions, the porous-effect parameter is further expressed as $\sigma = c_0\omega$. Following Yu and Chwang (1994), $c_0 = \rho b_0/v$ where v is the fluid's dynamic viscosity, b_0 designates the porosity coefficient. c_0 only depends on the design of the perforated plate. $c_0 = 0.5$ s/m is used in the subsequent computation.

The variation of the captured wave energy with respect to the peak wave period T_p is shown in Fig. 22. Three significant wave heights, i.e., $H_s = 1.0$ m, 1.5 m and 2.0 m, are considered. Those wave heights correspond to the operational sea states, as Ren et al.

(2020) suggested. Analogous results to those in Fig. 22 but for the standard deviation of the wave force and moment, denoted by S_d (F_x) and S_d (M_y) hereinafter, are given in Figs. 23 and 24. A quadratic relationship between H_s and W_c can be found. In the meantime, S_d (F_x) and S_d (M_y) grow linearly with H_s. When H_s = 2.0 m, the prominent peak of W_c is beyond 210 kW. It indicates that even though the size of the OWC is not large, i.e., R_e = 6.0 m and d = 3.0 m, the captured wave energy can still be an essential supplement to the hybrid system.

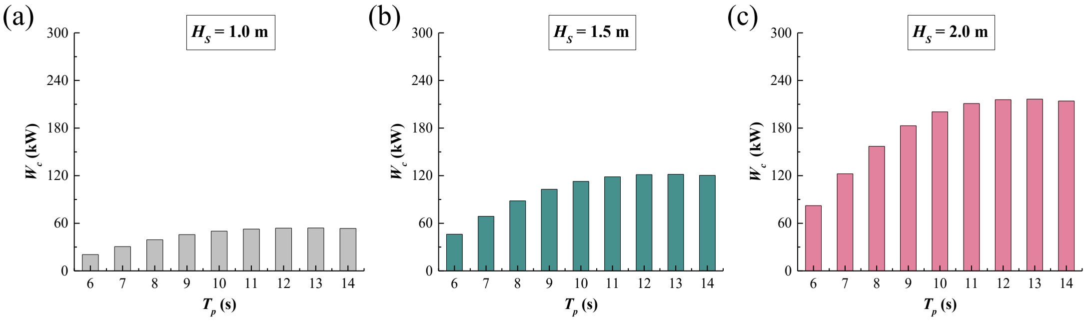

Fig. 22 Variation of the captured wave energy with respect to the peak wave period for c_0 = 0.5 s/m and b = 4 m: (a) H_s = 1.0 m, (b) H_s = 1.5 m and (c) H_s = 2.0 m.

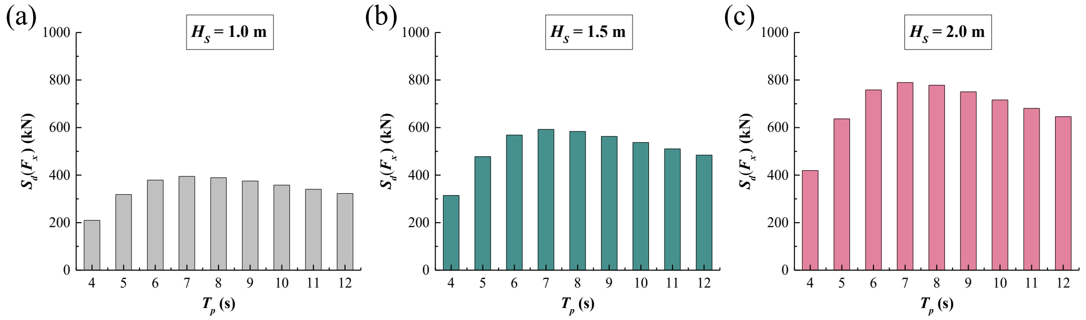

Fig. 23 Variation of the standard deviation of the horizontal wave force with respect to the peak wave period for c_0 = 0.5 s/m and b = 4 m: (a) H_s = 1.0 m, (b) H_s = 1.5 m and (c) H_s = 2.0 m.

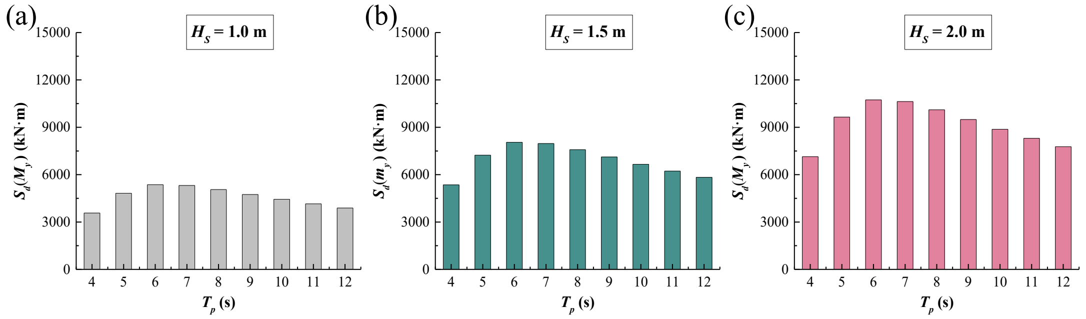

Fig. 24 Variation of the standard deviation of the bending moment with respect to the peak wave period for c_0 = 0.5 s/m and b = 4 m: (a) H_s = 1.0 m, (b) H_s = 1.5 m and (c) H_s = 2.0 m.

Numerical computation is then conducted for the case without the perforated plate, and the statistical results are shown in Fig. 25. In addition, the changing ratio is shown in Fig 26. The changing ratio is determined by ($S_{\mathrm{wo}} - S_{\mathrm{w}}$)/$S_{\mathrm{wo}}$, in which S_{w} represents the statistics results for the case with the perforated plate, while S_{wo} is for that without the plate. The changing ratio continues to decay as the peak wave period increases. In the long-period region, where wave energy harvesting is noticeable and becomes an important design consideration, the effect of the perforated plate is negligible. At T_p = 12 s and 13 s, which are the periods of the first two largest values of W_c, the changing ratios of W_c are 2.8% and 2.3%, respectively. In the short-period region, where the wave force and moment are significant and can impose a considerable threat to the system's safety, the presence of the plate has a remarkable effect. At T_p = 5 s and 6 s, the periods of the first two largest values of S_d (M_y), the changing ratios of S_d (M_y) are 15.03% and 8.89%, respectively. The corresponding changing ratios for S_d (F_x) are 12.27% and 5.92%, respectively. The above observation indicates that using the perforated plate can reduce the high wave force/moment in the low-period region while imposing negligible impact on the significant wave energy harvesting in the long-period region.

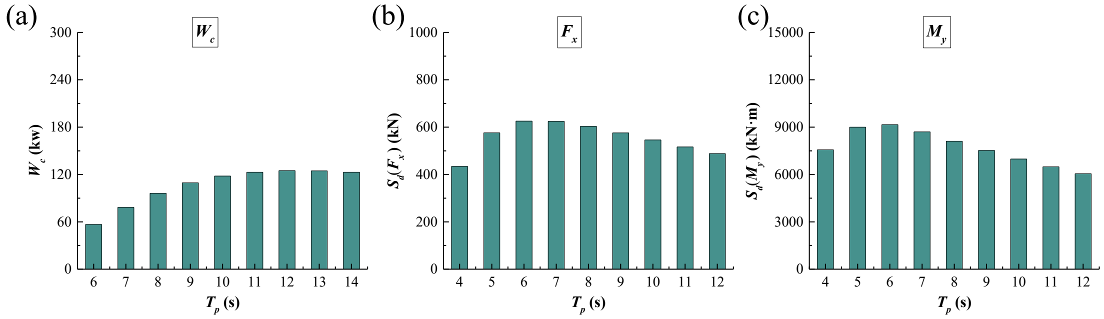

Fig. 25 Variation of the statistical results with respect to the peak wave period for H_s = 1.5 m when without the perforated plate: (a) W_c, (b) F_x and (c) M_y.

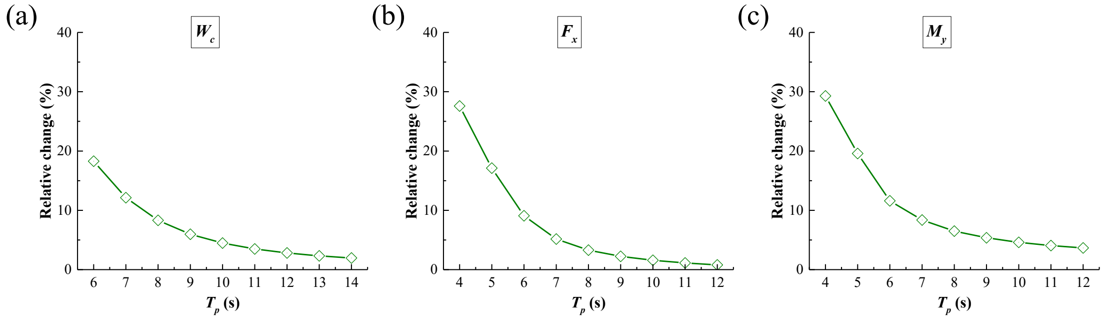

Fig. 26 Changing ratio of the statistical results between the cases with and without the perforated

plate: (a) W_c, (b) F_x and (c) M_y.

6. Conclusions

The functional performance of an annular OWC integrated into a monopile foundation is assessed. A submerged ring-shaped horizontal perforated plate is attached rigidly to the shell of the OWC chamber to mitigate the wave loads. Various hydrodynamic properties related to the system have been evaluated based on a newly developed solution. The main conclusions of this study are summarized as follows:

(1) Using a perforated plate can effectively reduce the system's horizontal wave force and bending moment. As the exterior radius of the perforated plate increases or the perforated plate is located at a lower submergence depth, its effect is more evident on the wave loads. The former is due to the wave scattering process affecting a broad region of the wave field around the system, and the latter is due to the wave energy concentration near the free surface.

(2) As the plate's porosity decreases, it becomes more effective in remitting the wave loads. When the porosity decreases further and approaches zero, the effect of wave energy dissipation by the plate gradually evolves into wave reflection. This can lead to apparent wave energy focusing in the vicinity of the plate and reinforcing the wave loads on the system.

(3) Remarkable resonant wave motions inside the chamber, namely $p = 0$, 1, 2 and 3 modes, have been found. Using a perforated plate can attenuate the wave motion inside the chamber.

(4) Investigation has been extended to irregular sea conditions. The perforated plate's effect gradually becomes less evident as the wave period increases. This is because long waves can better pass through porous media. Wave energy harvesting is significant in the long-period region. These properties are required to be considered as a priority in the design. The presence of the plate can reduce the high bending moment. The corresponding changing ratio is more excellent than 15%. Meanwhile, the effect on high wave energy harvesting is negligible. Numerical results illustrate the feasibility of making an insignificant effect on the high wave energy harvesting while reducing the high

wave loads by attaching a submerged horizontal perforated plate.

Acknowledgements

P. C. acknowledges support from the National Natural Science Foundation of China [Grant No. 51809037] and the Joint Funds of the National Natural Science Foundation of China [Grant No. U22A20242]. Y. L. acknowledges support from Grant-in-Aid for Early-Career Scientists (JSPS) [Grant No. JP22K14430] and Open Research Fund of State Key Laboratory of Coastal and Offshore Engineering (Dalian University of Technology) [Grant No. LP1815].

Appendix A

The following symbols are used in this paper:

A	incident wave amplitude;
a	= 3 m, radius of the monopile;
b_0	porosity coefficient;
c	sound speed in the air;
D	diameter of the turbine rotor;
d	submergence depth of the perforated plate;
f_x	amplitude of the horizontal wave force;
f_z	amplitude of the vertical wave force;
F_x	horizontal wave force;
F_z	vertical wave force;
g	gravitational acceleration;
H_m	modified Hankel function of the second kind of order m;
h	water depth;
I_m	modified Hankel function of the first kind of order m;
J_m	Bessel function of order m;
K_m	Hankel function of the first kind of order m;
κ_0	wave number;
κ_j	wave numbers for evanescent modes;
m_y	amplitude of the wave moment;
M_y	Wave moment;
N	rotational speed of the air turbine;
p_c	amplitude of the oscillating air pressure;
q_c	amplitude of the air volume flux;
R_b	Exterior radius of the perforated plate
R_e	Exterior radius of the chamber shell;
R_i	Interior radius of the chamber shell;

T	draft of the air chamber;
W_c	Absorbed wave energy;
χ	turbine parameter;
ϕ	velocity potential;
ϕ_j	velocity potential in the jth subdomain;
ϕ_I	incident potential;
η	free-surface elevation amplitude;
μ	chamber parameter;
μ_j	complex wave number satisfying a complex dispersion relation;
ρ	water density;
ρ_a	air density;
σ	porous-effect parameter;
ω	angular frequency;
Λ	pneumatic damping coefficient;
Ω_j	the jth fluid subdomain.

Appendix B

In the expression of the wave force (see Eq. (36)), the coefficients $I_{z,l}^1$, $I_{z,j}^2$ and $I_{z,j}^3$ are defined by:

$$I_{z,l}^1 = \left\{ \frac{\sinh\left[\mu_l (h-d)\right]}{\mu_l} \cdot \frac{\omega^2}{g} - \frac{\sinh\left[\mu_l (h-T)\right]}{\mu_l} \cdot \left[\frac{\omega^2}{g} \cosh(\mu_l d) - \mu_l \sinh(\mu_l d) \right] \right\} \cdot \frac{1}{\sqrt{M_l}}; \tag{A1a}$$

$$I_{z,j}^2 = \begin{cases} \dfrac{1}{\kappa_0} \cdot \dfrac{\sinh(\kappa_0 h) - \sinh\left[\kappa_0 (h-T)\right]}{\cosh(\kappa_0 h)} \cdot \dfrac{1}{\sqrt{N_0}}, & j = 0, \\ \dfrac{1}{\kappa_j} \cdot \dfrac{\sin(\kappa_j h) - \sin\left[\kappa_j (h-T)\right]}{\cos(\kappa_j h)} \cdot \dfrac{1}{\sqrt{N_j}}, & j \geq 1; \end{cases} \tag{A1b}$$

$$I_{z,j}^3 = \begin{cases} \dfrac{1}{\kappa_0} \cdot \tanh(\kappa_0 h) \cdot \dfrac{1}{\sqrt{N_0}}, & j = 0, \\ \dfrac{1}{\kappa_j} \cdot \tan(\kappa_j h) \cdot \dfrac{1}{\sqrt{N_j}}, & j \geq 1. \end{cases} \tag{A1c}$$

In addition, the functions $I_{r,l}^1(r)$, $I_{r,l}^2(r)$, $I_{r,k}^3(r)$ and $I_{r,k}^4(r)$ are defined by:

$$I_{r,l}^1(r) = \frac{r}{\mu_l} \left[\frac{J_1(\mu_l r) H_0(\mu_l R_e) - J_0(\mu_l R_e) H_1(\mu_l r)}{J_0(\mu_l R_b) H_0(\mu_l R_e) - J_0(\mu_l R_e) H_0(\mu_l R_b)} \right]; \tag{A2a}$$

$$I_{r,l}^2(r) = \frac{r}{\mu_l} \left[\frac{J_0(\mu_l R_b) H_1(\mu_l r) - J_1(\mu_l r) H_0(\mu_l R_b)}{J_0(\mu_l R_b) H_0(\mu_l R_e) - J_0(\mu_l R_e) H_0(\mu_l R_b)} \right]; \tag{A2b}$$

$$I_{r,k}^{3}(r)=\begin{cases}\dfrac{r^{2}\left(2\ln r-2\ln R_{i}-1\right)}{4\ln\left(R_{e}/R_{i}\right)}, & k=0,\\[2ex] \dfrac{r}{\lambda_{k}}\cdot\dfrac{I_{1}\left(\lambda_{k}r\right)K_{0}\left(\lambda_{k}R_{i}\right)+I_{0}\left(\lambda_{k}R_{i}\right)K_{1}\left(\lambda_{k}r\right)}{I_{0}\left(\lambda_{k}R_{e}\right)K_{0}\left(\lambda_{k}R_{i}\right)-I_{0}\left(\lambda_{k}R_{i}\right)K_{0}\left(\lambda_{k}R_{e}\right)}, & k>0;\end{cases}\tag{A2c}$$

$$I_{r,k}^{4}(r)=\begin{cases}-\dfrac{r^{2}\left(2\ln r-2\ln R_{e}-1\right)}{4\ln\left(R_{e}/R_{i}\right)}, & k=0,\\[2ex] \dfrac{r}{\lambda_{k}}\cdot\dfrac{-I_{0}\left(\lambda_{k}R_{e}\right)K_{1}\left(\lambda_{k}r\right)-I_{1}\left(\lambda_{k}r\right)K_{0}\left(\lambda_{k}R_{e}\right)}{I_{0}\left(\lambda_{k}R_{e}\right)K_{0}\left(\lambda_{k}R_{i}\right)-I_{0}\left(\lambda_{k}R_{i}\right)K_{0}\left(\lambda_{k}R_{e}\right)}, & k>0.\end{cases}\tag{A2d}$$

Reference

Arshad M, O'Kelly B C. Analysis and design of monopile foundations for offshore wind-turbine structures. Marine Georesources & Geotechnology, 2016, 34(6): 503-525.

Chwang A T. A porous-wavemaker theory. Journal of Fluid Mechanics, 1983, 132: 395-406.

Cho I H, Kim M H. Wave absorbing system using inclined perforated plates. Journal of Fluid Mechanics, 2008, 608: 1-20.

Cho I H, Kim M H. Transmission of oblique incident waves by a submerged horizontal porous plate. Ocean Engineering, 2013, 61: 56-65.

Cheng Z S, Wen T R, Ong M C, Wang K. Power performance and dynamic responses of a combined floating vertical axis wind turbine and wave energy converter concept. Energy, 2019, 171: 190-204.

Cong P W, Teng B, Bai W, Liu Y Y. Wave power absorption by an oscillating water column (OWC) device of annular cross-section in a combined wind-wave energy system. Applied Ocean Research, 2021, 107: 102499.

Cong P W, Teng B, Liu Y Y, Ning D Z. A numerical approach for hydrodynamic performance evaluation of multi-degree-of-freedom floating oscillating water column (OWC) devices. Journal of Fluids and Structures, 2022, 114: 103730.

Dimitrios N K, Georgios M K, Dimitrios I M, Takvor H S, Stylianos Polyzos, Thomas P M, Spyros G Voutsinas, Spyridon A M. REFOS: a renewable energy multi-purpose floating offshore system. Energies, 2021, 14(11): 3126.

Evans D V, Porter R. Efficient calculation of hydrodynamic properties of OWC-Type devices. Journal of Offshore Mechanics and Arctic Engineering, 1997, 119(4): 210-218.

Evans D V, Peter M A. Asymptotic reflection of linear water waves by submerged horizontal porous plates. Journal of Engineering Mathematics, 2011, 69: 135-154.

Gao Q, Yuan R, Ertugrul N, Ding B Y, Hayward J A, Li Y. Analysis of energy variability and costs for offshore wind and hybrid power unit with equivalent energy storage system. Applied Energy, 2023, 342: 121192.

Huang Z H, Li Y C, Liu Y. Hydraulic performance and wave loadings of perforated/slotted coastal structures: A review. Ocean Engineering, 2011, 38(10): 1031-1053.

Hu J, Zhou B Z, Vogel C, Liu P, Willden R, Sun K, Zang J, Geng J, Jin P, Cui, L, Jiang B, Collu M. Optimal design and performance analysis of a hybrid system combing a floating wind platform and wave energy converters. Applied Energy, 2020, 269: 114998.

Jiang Z Y, Gao Z, Ren Z R, Li Y, Duan L. A parametric study on the final blade installation process for monopile wind turbines under rough environmental conditions. Engineering Structures, 2018, 172: 1042-1056.

Karimirad M. Offshore energy structures: for wind power, wave energy and hybrid marine platforms. Springer, 2014.

Li Y C, Liu Y, Teng B. Porous effect parameter of thin permeable plates. Coastal Engineering Journal, 2006, 48(04): 309-336.

Liu Y, Li Y C, Teng B, Dong S. Wave motion over a submerged breakwater with an upper horizontal porous plate and a lower horizontal solid plate. Ocean Engineering, 2008, 35(16): 1588-1596.

Liu Y, Li H J, Li Y C. A new analytical solution for wave scattering by a submerged horizontal porous plate with finite thickness. Ocean Engineering, 2012, 42: 83-92.

Li Y M, Ong M C, Wang K, Li L B, Cheng Z S. Power performance and dynamic responses of an integrated system with a semisubmersible wind turbine and four torus-shaped wave energy converters. Ocean Engineering, 2022a, 259: 111810.

Li Y N, Liu S Z, Xu C L, Li D M, Shi H D. Experimental study on the cylindrical oscillating water column device. Ocean Engineering, 2022b, 246: 110523.

Li Y, Zhao X L, Geng J, Mackay E, Johanning L. Wave scattering by a vertical cylinder with a submerged porous plate: Further analysis. Ocean Engineering, 2022c, 259: 111711.

Liang H, Zheng S, Shao Y, Chua K H, Choo Y S, Greaves D. Water wave scattering by impermeable and perforated plates. Physics of Fluids, 2021, 33(7).

Liang H, Zheng S, Magee A R, Greaves D. Water wave interactions with perforated elastic disks: Quadratic pressure discharge condition. Physical Review Fluids, 2022, 7(5): 054802.

Luan C, Michailides C, Gao Z, Moan T. Modeling and analysis of a 5 MW semisubmersible wind turbine combined with three flap-type wave energy converters. In Proceedings of the 33rd International Conference on Offshore Mechanics and Arctic Engineering. American Society of Mechanical Engineers, 2014, San Francisco, California, USA.

Mavrakos S A. Wave loads on a stationary floating bottomless cylindrical body with finite wall thickness. Applied Ocean Research, 1985, 7(4): 213-224.

Martins-Rivas H, Mei C C. Wave power extraction from an oscillating water column at the tip of a breakwater. Journal of Fluid Mechanics, 2009, 626: 395-414.

Muliawan M J, Karimirad M, Moan T. Dynamic response and power performance of a combined spar-type floating wind turbine and coaxial floating wave energy converter. Renewable Energy, 2013, 50: 47-57.

Michailides C, Gao Z, Moan T. Experimental study of the functionality of a semisubmersible wind turbine combined with flap-type Wave Energy Converters. Renewable energy, 2016a, 93: 675-690.

Michailides C, Gao Z, Moan T. Experimental and numerical study of the response of the offshore combined wind/wave energy concept SFC in extreme environmental conditions. Marine Structures, 2016b, 50: 35-54.

Michele S, Renzi E, Perez-Collazo C, Greaves D, Iglesisa G. Power extraction in regular and random waves from an OWC in hybrid wind-wave energy systems. Ocean Engineering, 2019, 191: 106519.

Meng F T, Sergiienko N, Ding B Y, Zhou B Z, Silva LSP Da, Cazzolato B, Li Y. Co-located offshore wind–wave energy systems: Can motion suppression and reliable power generation be achieved simultaneously? Applied Energy, 2023, 331: 120373.

Meylan M H, Bennetts L G, Peter M A. Water-wave scattering and energy dissipation by a floating porous elastic plate in three dimensions. Wave Motion, 2017, 70: 240-250.

Mohapatra S C, Sahoo T, Soares C G. Surface gravity wave interaction with a submerged horizontal flexible porous plate. Applied Ocean Research, 2018, 78: 61-74.

Perez-Collazo C, Greaves D, Iglesias G. Hydrodynamic response of the WEC sub-system of a novel hybrid wind-wave energy converter. Energy Conversion and Management, 2018, 171: 307-325.

Poguluri S K, Kim J, George A, Cho I H. Wave interaction with horizontal multilayer porous plates. Journal of Waterway, Port, Coastal, and Ocean Engineering, 2022, 148(5): 04022016.

Ren N X, Ma Z, Shan B H, Ning D Z, Ou J P. Experimental and numerical study of dynamic responses of a new combined TLP type floating wind turbine and a wave energy converter under operational conditions. Renewable Energy, 2020, 151: 966-974.

Sarmiento J, Iturrioz A, Ayllón V, Guanche R, Losada I J. Experimental modelling of a multi-use floating platform for wave and wind energy harvesting. Ocean Engineering, 2019, 173: 761-773.

Vijay K G, Nishad C S, Neelamani S, Sahoo T. Gravity wave interaction with a wave attenuating system. Applied Ocean Research, 2020, 101: 102206.

Wang X F, Zeng X W, Yang X, Li J L. Seismic response of offshore wind turbine with hybrid monopile foundation based on centrifuge modelling. Applied energy, 2019, 235: 1335-1350.

Yu X P, Chwang A T. Water waves above submerged porous plate. Journal of Engineering Mechanics, 1994, 120(6): 1270-1282.

Zhao FF, Bao W G, Kinoshita T, Itakura H. Theoretical and experimental study on a porous cylinder floating in waves. Journal of Offshore Mechanics and Arctic Engineering, 2011, 133: 011301.

Zhao F F, Zhang T Z, Wan R, Huang L Y, Wang X X, Bao W G. Hydrodynamic loads acting on a circular porous plate horizontally submerged in waves. Ocean Engineering, 2017, 136: 168-177.

Zhang D H, Chen Z, Liu X D, Sun J L, Yu H, Zeng W J, Ying Y, Sun Y, Cui, L, Yang S J, Qian P, Si Y L. A coupled numerical framework for hybrid floating offshore wind turbine and oscillating water column wave energy converters. Energy Conversion and Management, 2022, 267: 115933.

Zheng S M, Meylan M H, Zhu G X, Greaves D, Iglesias G. Hydroelastic interaction between water waves and an array of circular floating porous elastic plates. Journal of Fluid Mechanics, 2020a, 900: A20.

Zheng S M, Meylan M H, Greaves D, Iglesias G. Water-wave interaction with submerged porous elastic disks. Physics of Fluids, 2020b, 32(4).

Zheng S M, Liang H, Michele S, Greaves D. Water wave interaction with an array of submerged circular plates: Hankel transform approach. Physical Review Fluids, 2023, 8(1): 014803.

Zhou Y, Ning D Z, Shi W, Johanning L, Liang D F. Hydrodynamic investigation on an OWC wave energy converter integrated into an offshore wind turbine monopile. Coastal Engineering, 2020, 162: 103731.